Inorganic Chemistry

Article

pubs.acs.org/IC

# Experimental and Theoretical Study of $SbPO_4$ under Compression

André Luis de Jesus Pereira,*[,†,‡] David Santamaría-Pérez,[§] Rosário Vilaplana,[∥] Daniel Errandonea,[§] Catalin Popescu,[⊥] Estelina Lora da Silva,[†] Juan Angel Sans,[†] Juan Rodríguez-Carvajal,[#] Alfonso Muñoz,[▽] Plácida Rodríguez-Hernández,[▽] Andres Mujica,[▽] Silvana Elena Radescu,[▽] Armando Beltrán,[●] Alberto Otero de la Roza,[○] Marcelo Nalin,[△] Miguel Mollar,[†] and Francisco Javier Manjón*[,†]

[†]Instituto de Diseño para la Fabricación y Producción Automatizada, MALTA Consolider Team, Universitat Politècnica de València, València, Spain

[‡]Grupo de Pesquisa de Materiais Fotonicos e Energia Renovável-MaFER, Universidade Federal da Grande Dourados, Dourados, Mato Grosso do Sul, Brazil

[§]Departament de Física Aplicada-ICMUV, MALTA Consolider Team, Universitat de València, Burjassot, Spain

[∥]Centro de Tecnologías Físicas, MALTA Consolider Team, Universitat Politecnica de València, València 46022, Spain

[⊥]CELLS-ALBA Synchrotron Light Facility, 08290 Cerdanyola, Barcelona, Spain

[#]Institut Laue-Langevin, 71 Avenue des Martyrs, CS 20156, 38042 Grenoble Cedex 9, France

[▽]Departamento de Física, Instituto de Materiales y Nanotecnología, MALTA Consolider Team, Universidad de La Laguna, Tenerife, Spain

[●]Departament de Química Física i Analítica, MALTA Consolider Team, Universitat Jaume I, Castelló, Spain

[○]Departamento de Química Física y Analítica, MALTA Consolider Team, Universidad de Oviedo, 33006 Oviedo, Spain

[△]Instituto de Quimica, Departamento de Química Geral e Inorgânica, UNESP-Campus de Araraquara, São Paulo, Brazil

Supporting Information

**ABSTRACT:** $SbPO_4$ is a complex monoclinic layered material characterized by a strong activity of the nonbonding lone electron pair (LEP) of Sb. The strong cation LEP leads to the formation of layers piled up along the *a* axis and linked by weak Sb−O electrostatic interactions. In fact, Sb has 4-fold coordination with O similarly to what occurs with the P−O coordination, despite the large difference in ionic radii and electronegativity between both elements. Here we report a joint experimental and theoretical study of the structural and vibrational properties of $SbPO_4$ at high pressure. We show that $SbPO_4$ is not only one of the most compressible phosphates but also one of the most compressible compounds of the $ABO_4$ family. Moreover, it has a considerable anisotropic compression behavior, with the largest compression occurring along a direction close to the axis and governed by the compression of the LEP and the weak interlayer Sb−O bonds. The strong compression along the *a* axis leads to a subtle modification of the monoclinic crystal structure above 3 GPa, leading from a 2D to a 3D material. Moreover, the onset of a reversible pressure-induced phase transition is observed above 9 GPa, which is completed above 20 GPa. We propose that the high-pressure phase is a triclinic distortion of the original monoclinic phase. The understanding of the compression mechanism of $SbPO_4$ can aid in understanding the importance of the ion intercalation and catalytic properties of this layered compound.

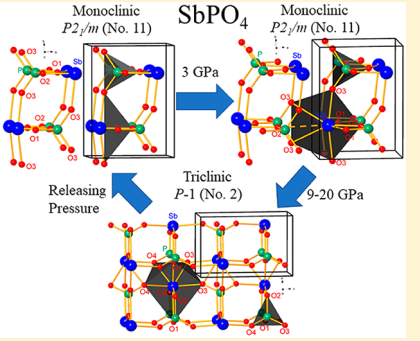


## 1. INTRODUCTION

Inorganic functional materials composed of antimony, such as antimony orthophosphate ($SbPO_4$), are receiving considerable attention from the scientific community, due to their potential applications in different areas. The excellent optical properties of antimony-based glasses, such as the high-linearity refractive index[1,2] and the large transmittance window from the ultraviolet (UV) to infrared (IR) regions,[3] enables its application as optical fibers, allowing its use in photonic applications.[4] The remarkable optical properties of $SbPO_4$ have also drawn a great deal of attention as a photocatalyst under UV light irradiation.[5,6] Moreover, since $SbPO_4$ belongs to a class of phosphates with a very stable layered structure, where ions can be intercalated between its layers, many research groups have studied its ion-exchange characteristics[7] and respective potential as an anode in lithium-ion batteries.[8,9]

**Received:** July 26, 2019





DOI: 10.1021/acs.inorgchem.9b02268
Inorg. Chem. XXXX, XXX, XXX−XXX

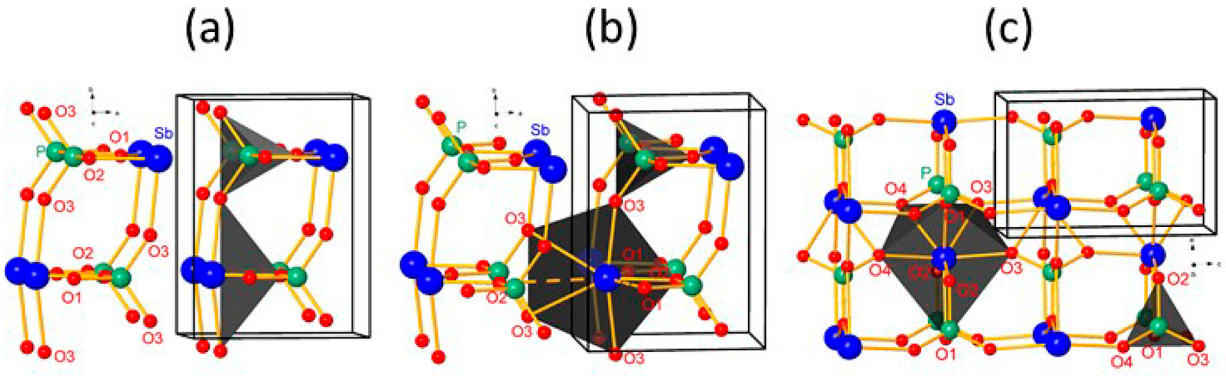


**Figure 1.** (a) 2D crystalline structure of monoclinic $SbPO_4$ at room pressure. The layered structure is composed of P atoms which are 4-fold coordinated to O in the $sp^3$ tetrahedral arrangement and Sb atoms which are 4-fold coordinated to O in a trigonal-bipyramidal fashion. The distortion of the Sb polyhedron is caused by the strong LEP, which points to the interlayer space (not shown). (b) 3D crystalline structure of monoclinic $SbPO_4$ at 3 GPa, showing the (4 + 2)-fold coordination for Sb if one includes not only four Sb−O distances below 2.2 Å but also two Sb−O distances just below 2.6 Å (see Figure 6). Dashed lines show two other Sb−O distances above 2.8 Å that do not enter the Sb coordination. The position of the Sb LEP can be considered intermediate between the two dashed lines. (c) 3D crystalline structure of triclinic $SbPO_4$ at 18 GPa showing a (4 + 2 + 1)-fold coordination for Sb in a distorted-dodecahedral fashion (Sb−O distances are between 2.0 and 2.7 Å) and 4-fold coordinated P atoms in a tetrahedral $sp^3$ arrangement. Large blue balls represent Sb atoms, medium green balls represent P atoms, and small red balls represent O atoms.

$SbPO_4$ is an $A^{3+}B^{5+}O_4$ compound with a layered structure that crystallizes in the monoclinic space group $P2_1/m$ (No. 11), which is isostructural with $SbAsO_4$[10] and belongs to the same space group as the polymorph $BiPO_4$-III.[11,12] The low-pressure (LP) structure of $SbPO_4$ is composed of a combination of regular $PO_4$ tetrahedra and $SbO_4E$ polyhedra disposed in a trigonal-bipyramidal fashion, where E refers to the nonbonding lone electron pair (LEP) of Sb (see Figure 1a). For both $BiPO_4$-III and $SbPO_4$, P is 4-fold coordinated at room pressure; however, while $SbPO_4$ is a layered compound, $BiPO_4$-III is not, and therefore these are not isostructural compounds. At room pressure, the Bi ion belonging to the $BiPO_4$-III compound features a 6-fold coordination, whereas Sb has only a 4-fold coordination for $SbPO_4$. The difference between both compounds is the result of the stronger LEP of Sb(III) in comparison to the LEP of Bi(III): i.e. the strong Sb LEP prevents the formation of Sb−O bonds in either direction, thus leading to the formation of layers in $SbPO_4$ unlike what occurs for $BiPO_4$-III. The layers of $SbPO_4$ are piled up along the *a* axis and are linked by weak Sb−O electrostatic interactions.

The vibrational properties of $SbPO_4$ have been studied at room pressure by Raman and IR spectroscopy,[13−16] but a limited amount of information has been provided. For instance, the classification and symmetry assignment of all vibrational modes at the Brillouin zone (BZ) center (Γ), the phonon dispersion curves (PDCs), and the phonon density of states (PDOS) have not been reported even at room pressure.

High-pressure (HP) studies of several $APO_4$ orthophosphates have been reported in the literature: i.e., where zircon- and monazite-type phosphates have been broadly studied.[17−27] The pressure-induced structural sequence has been understood, with several new HP phases discovered and their crystal structures solved. In addition, the influence of pressure in the vibrational properties and unit-cell parameters has been well established. The number of HP studies carried out has also helped to unveil the existing relationship between the response under compression of the microscopic and macroscopic properties of these materials. In particular, the compressibility has been explained in terms of polyhedral compressibilities.[23] Moreover, the studies of phosphates under extreme conditions have been recently extended to compounds with different crystal structures in comparison to zircon or monazite. In particular, phosphates with the olivine structure as well as complex phosphates, such as $K_2Ce(PO_4)_2$ and isomorphic compounds, have been characterized under HP.[28,29] Finally, metastable polymorphs of $BiPO_4$,[18] spin-Peierls distorted $TiPO_4$,[30] and $CrVO_4$-type phosphates[31] have also been recently studied at HP. Phase transitions (PTs) driven by compression have been reported for all these compounds, with a common feature found that the PTs are always first-order, involving a collapse of the volume and the breaking and formation of chemical bonds. Moreover, HP has been found to be a successful route to pentacoordinated phosphorus, which is achieved at a pressure of 46 GPa in $TiPO_4$.[30] In contrast with all the phosphates mentioned above, the HP behavior of $SbPO_4$ has not yet been explored. As this structure is a layered compound and Sb possesses a strong LEP, $SbPO_4$ is an ideal candidate for an unusual HP behavior with high compressibility and with subtle PTs at pressure much lower than that found for other $APO_4$ orthophosphates.

In this work, we report a joint experimental and theoretical study of the structural and vibrational properties of $SbPO_4$ at HP by means of X-ray diffraction (XRD) and Raman scattering (RS) measurements combined with ab initio calculations. We will show that $SbPO_4$ is one of the most compressible phosphates and $ABO_4$ compounds. Moreover, it exhibits a considerable anisotropic behavior due to a high nonlinear compression, mainly along the *a* axis, as shown by the respective compressibility tensor. Additionally, we will show that our measurements and calculations are compatible with the existence of an isostructural phase transition (IPT) around 3 GPa and a reversible PT above 9 GPa, which is completed around 20 GPa. After the study of several candidates for the HP phase of $SbPO_4$ on the basis of an updated Bastide diagram[20,32] for $ABO_4$ compounds containing cations with LEPs, such as $As^{3+}$, $Sb^{3+}$, $Bi^{3+}$, $Sn^{2+}$, and $Pb^{2+}$, we propose a triclinic distortion of the original monoclinic phase as the HP phase above 9 GPa. The experimental and theoretical vibrational modes of both LP and HP phases at different pressures will be shown, and a tentative assignment of the symmetry of each observed Raman-active mode will be provided. This work helps to better understand how layered $SbPO_4$ behaves under compression


DOI: 10.1021/acs.inorgchem.9b02268
Inorg. Chem. XXXX, XXX, XXX−XXX

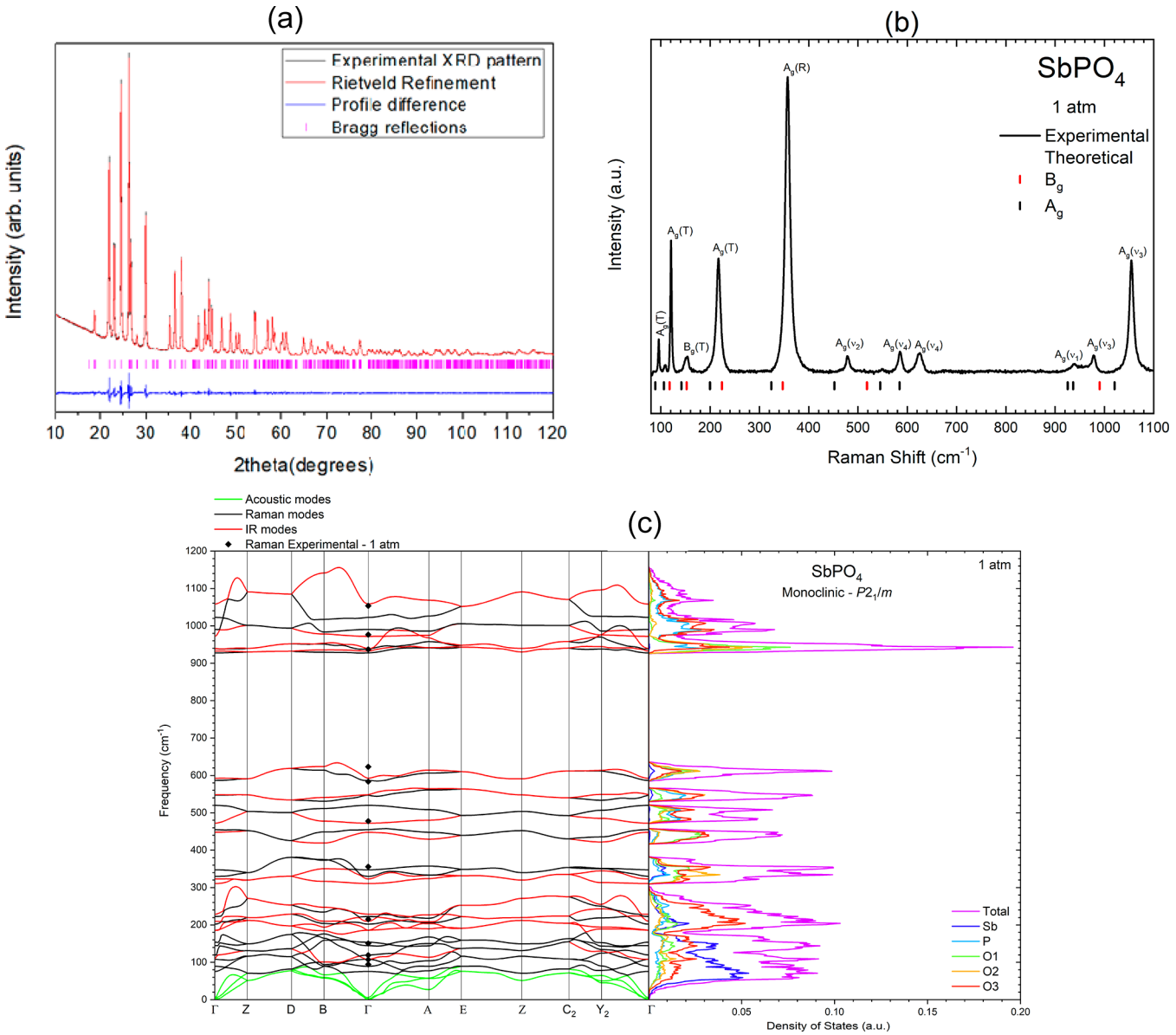


**Figure 2.** Characterization of monoclinic $SbPO_4$ at room pressure: Experimental powder XRD pattern (a) and RS spectrum (b) and theoretical PDC and PDOS (c). The bottom marks in (a) show the angle of diffraction peaks and residuals of Rietveld refinement of the XRD data. In (b) we have added a tentative mode assignment based in the theoretical results and the pressure evolution of these vibrational modes. The bottom marks in (b) show the frequencies of the Raman-active modes theoretically predicted at 0 GPa. The notations T, R, $\nu_1$, $\nu_2$, $\nu_3$, and $\nu_4$ refer to the main character of translation, rotation, or internal modes of the $PO_4$ units, respectively.

and provides clues to design better photocatalysts and better intercalated compounds with enhanced ion-exchange characteristics on the basis of this phosphate. This work helps us understand the behavior of the layered $SbPO_4$ under compression, thus providing insights to direct and improve the design of similar photocatalysts and intercalated compounds with enhanced ion-exchange characteristics.

## 2. EXPERIMENTAL METHOD

Synthetic $SbPO_4$ powders used in the present experiments were synthesized by Nalin and co-workers.[2−4] Energy dispersive X-ray spectroscopy (EDS) analyses performed with an Oxford Instruments detector coupled to a JEOL JSM6300 scanning electron microscope showed a good stoichiometry and no appreciable impurities.

The structural characterization of powders at room pressure was carried out by XRD measurements performed with a Rigaku Ultima IV diffractometer using Cu K$\alpha$ (1.5406 and 1.5443 Å for K$\alpha_1$ and K$\alpha_2$, respectively) as the incident radiation source. Traces of other phases or of $Sb_2O_3$ were not detected. Vibrational characterization of powders at room pressure was carried out by RS measurements performed with a Horiba Jobin Yvon LabRAM HR UV microspectrometer, equipped with a thermoelectrically cooled multichannel charge-coupled device detector and a 1200 grooves/mm grating that allows a spectral resolution of better than 3 $cm^{-1}$. The signal was collected in backscattering geometry on excitation with a 532 nm laser with a power of less than 10 mW. Phonons were analyzed by fitting Raman peaks with a Voigt profile fixing the Gaussian line width (2.4 $cm^{-1}$) to the experimental setup resolution. RS experiments allowed us also to confirm that the samples contained only a pure phase.

Powder angle-dispersive HP-XRD measurements were performed at room temperature in three different experiments. Initially, we performed two experiments (called run 1 and run 2) using an Xcalibur diffractometer with the lines K$\alpha_1$ and K$\alpha_2$ of a Mo source with $\lambda$ = 0.7093 and 0.7136 Å, respectively. The sample was loaded with a 16/3/1 methanol/ethanol/water mixture in a Merrill-Bassett-type


DOI: 10.1021/acs.inorgchem.9b02268
Inorg. Chem. XXXX, XXX, XXX−XXX

diamond anvil cell (DAC) with diamond culets of 400 $\mu$m in diameter.[33] A third powder angle-dispersive HP-XRD experiment (run 3) was performed up to 15.2 GPa at the BL04-MSPD beamline at the ALBA synchrotron facility.[34] This beamline is equipped with Kirkpatrick–Baez mirrors to focus the monochromatic beam and a Rayonix CCD detector with a 165 mm diameter active area and was operated with a wavelength of 0.4246 Å. In the first two experiments, the pressure was determined by the luminescence of small ruby chips evenly distributed in the pressure chamber,[35] while in the third experiment the pressure was determined with the equation of state (EoS) of copper.[36] Integration of 2D diffraction images was performed with Dioptas software,[37] while structural analysis was performed by Rietveld and Le Bail refinements using the FullProf[38] and PowderCell[39] program packages. In all of the experiments the DAC loading was performed, taking care to avoid sample bridging with the gasket.[40]

Finally, unpolarized HP-RS measurements up to 24.5 GPa were performed with the Horiba Jobin Yvon LabRAM HR UV microspectrometer previously mentioned. The sample was loaded with a 16/3/1 methanol/ethanol/water mixture in a membrane-type DAC, and the pressure was determined by the ruby luminescence method.[35] In the pressure range covered by Raman and XRD experiments the pressure was determined with an accuracy of 0.1 GPa.

## 3. THEORETICAL DETAILS

Ab initio calculations were performed within the framework of density functional theory (DFT)[41] to study the structural, vibrational, and elastic properties of $SbPO_4$ under pressure. Simulations were carried out with the Vienna ab initio simulation package (VASP)[42] using the projector augmented wave (PAW) pseudopotentials.[43] The PAW scheme replaces core electrons by smoothed pseudovalence wave functions considering the full nodal character of the all-electron charge density in the core region. The set of plane waves employed was extended up to a kinetic energy cutoff of 520 eV because of the presence of oxygen in $SbPO_4$. The generalized gradient approximation (GGA) was used for the description of the exchange-correlation energy within the PBEsol prescription.[44] The BZ of the monoclinic and the other analyzed structures of $SbPO_4$ were sampled with dense Monkhorst–Pack grids of special $k$ points.[45] A high convergence of 1–2 meV per formula unit in the total energy is achieved with the cutoff energy and the $k$-point sampling employed. This ensures an accurate calculation of the forces on atoms. At a set of selected volumes, the structure was fully relaxed to the optimized configuration through the calculation of the forces on the atoms and the stress tensor until the forces on the atoms were smaller than 0.005 eV/Å and the deviations of the stress tensor from a diagonal hydrostatic form were lower than 0.1 GPa.

Lattice-dynamics calculations were performed to study the phonons at the $\Gamma$ point of the BZ using the direct force constant approach (or supercell method). The diagonalization of the dynamic matrix provides the frequency and symmetry of the phonon modes. In order to obtain the PDCs along high-symmetry directions of the BZ and the PDOS, similar calculations were performed using appropriate supercells ($2 \times 2 \times 2$), which allow the PDCs at $k$ points to be obtained commensurate with the supercell size.[46] Finally, in order to study the HP mechanical stability of $SbPO_4$, the elastic stiffness constants were determined employing the stress theorem.[47] The optimized structures were strained, at different pressures, considering their symmetry.[48]

In order to analyze the Sb–O interatomic interactions of $SbPO_4$ at different pressures, we computed the electron density and its Laplacian at the Sb–O bond critical points using the VASP code and the CRITIC2 program.[49] The CRITIC2 code implements the quantum theory of atoms in molecules (QTAIM).[50] Within this theory, the one-saddle critical points of the electron density (bond critical points, BCPs), and their corresponding atomic interaction lines (bond paths), determine which atoms are bonded to which. In addition, the value of $\rho$ at the BCP correlates with the strength of the bond between two nuclei, provided the comparison is restricted to pairs of atoms of the same species. The Laplacian of the charge density at the BCP, $\nabla^2\rho(\mathbf{r})$ = 0, can be used to determine the covalent (if $\nabla^2\rho(\mathbf{r}) < 0$) character of the bond. We note that the charge density computed from the present PAW-DFT calculations using VASP solely contains the valence states; consequently, the calculated charge density values are only relevant for distances larger than the PAW radius of each atom (far enough from the core). However, it is this region where the BCPs appear and therefore the analysis of the density can still be used to characterize the Sb–O bond. We also performed an analysis of the electron localization function (ELF) along the Sb–O bonds. For the ELF analysis, we used the Elk software[51] version 6.3.2 with structural parameters obtained from the VASP optimization. The Elk software provides all-electron full-potential linearized augmented plane-wave (FPLAPW) calculations. We used a $4 \times 4 \times 4$ uniform grid for the reciprocal space sampling, a $R_{min} \times K_{max}$ value equal to 7.0, and a $G_{max}$ value for the interstitial expansion of the density and potential equal to 22.0 au. To have smoother ELF profiles, we increased the number of radial points inside the muffin tins to 1000, except in the 20.8 GPa case, where this causes SCF convergence difficulties.

## 4. RESULTS

**4.1. Structural and Vibrational Properties under Ambient Conditions.** The XRD diffractogram of $SbPO_4$ at room pressure is shown in Figure 2a. Rietveld refinement of the XRD pattern was performed using, as an initial model, the monoclinic $P2_1/m$ (space group No. 11) structure of $SbPO_4$ reported in the literature.[9] The refined parameters were the overall scale factor, the zero shift, the cell parameters, the pseudo-Voigt profile function with terms to account for the reflection anisotropic broadening (including anisotropic microstrains), the fractional atomic coordinates, and the background. The Rietveld refinement yielded the following lattice parameters at 1 atm $a$ = 5.10303(4) Å, $b$ = 6.77210(3) Å, $c$ = 4.74424(3) Å, and $\beta$ = 94.6089(4)°, the unit-cell volume $V_0$ = 163.422(2) Å$^3$, and the atomic coordinates collected in Table 1.

**Table 1. Atomic Coordinates of the Monoclinic $P2_1/m$ (Space Group No. 11) Structure of $SbPO_4$ under Ambient Conditions Obtained by Rietveld Refinement**[a]

| atom | Wyckoff position | $x$ | $y$ | $z$ |
|---|---|---|---|---|
| Sb | 2e | 0.18091(13) | 0.25 | 0.20633(14) |
| P | 2e | 0.6120(4) | 0.25 | 0.7215(5) |
| O1 | 2e | 0.3382(10) | 0.25 | 0.8346(10) |
| O2 | 2e | 0.5520(8) | 0.25 | 0.3997(9) |
| O3 | 4f | 0.7714(7) | 0.0712(4) | 0.8179(7) |

[a]The lattice parameters are $a$ = 5.10303(4) Å, $b$ = 6.77210(3) Å, $c$ = 4.74424(3) Å, and $\beta$ = 94.6089(4)°, with a unit cell volume $V_0$ = 163.422(2) Å$^3$.

These values agree with values reported in the literature: $a$ = 5.0868, $b$ = 6.7547 Å, $c$ = 4.7247 Å, $\beta$ = 94.66°, and $V_0$ = 161.8 Å$^3$.[11] Our experimental values agree with those from our own ab initio calculations (see Table S1 in the Supporting Information). We have found that the theoretical $V_0$ underestimates the experimental $V_0$ by only 0.4%, a value that is within the uncertainty in GGA-PBESol calculations.

At room pressure, the monoclinic structure of $SbPO_4$ has one Sb, one P, and three O atoms at independent Wyckoff sites: all atoms are at 2e ($x$, 1/4, $z$) sites except for one O, which is at a 4f ($x$, $y$, $z$) site. Therefore, the monoclinic structure has 11 free atomic parameters. For this structure, P atoms are 4-fold coordinated by O atoms and form regular tetrahedra with the P atom in the center and with P–O bond lengths ranging from 1.509(4) to 1.536(6) Å. On the other hand, Sb atoms are 4-fold unilaterally coordinated by O atoms and form a $SbO_4E$


DOI: 10.1021/acs.inorgchem.9b02268
Inorg. Chem. XXXX, XXX, XXX–XXX

polyhedron in a trigonal-bipyramidal fashion with the Sb−O bond lengths ranging from 2.000(6) to 2.193(3) Å (see Figure 1a). $PO_4$ tetrahedra and $SbO_4E$ polyhedra are connected by their edges, so that each $PO_4$ unit is linked to four $SbO_4E$ units and each $SbO_4E$ unit is linked to four $PO_4$ units. The $PO_4$ and $SbO_4E$ units are repeated along the [010] and [001] directions, forming layers along the [100] direction. As was observed on other Sb-based and Bi-based sesquioxides and sesquichalcogenides,[52−56] the presence of a strong nonbonding cation LEP in $SbPO_4$ causes a distortion in the structure that usually leads to a layered structure.

With regard to the lattice dynamics of $SbPO_4$, Figure 2b shows the experimental RS spectrum of $SbPO_4$ observed at room pressure. The RS spectrum accounts for 13 peaks at room pressure and is dominated by a strong mode close to 356 $cm^{-1}$. In fact, our RS spectrum is similar to the only one that has been published up to our knowledge[15] and is similar in appearance to that of $BiPO_4$-III.[12] Group theoretical considerations of the $P2_1/m$ structure yield 36 normal modes of vibration at Γ, whose mechanical decomposition is[57]

$$\Gamma = 11A_g(R) + 7B_g(R) + 6A_u(IR) + 9B_u(IR) + A_u + 2B_u$$

where the $A_g$ and $B_g$ modes are Raman-active (R) and $A_u$ and $B_u$ are infrared-active (IR), except for one $A_u$ and two $B_u$ modes that are the three acoustic modes. Therefore, the 33 optical modes are divided into 18 Raman-active modes ($\Gamma_{Raman} = 11A_g + 7B_g$) and 15 IR-active modes ($\Gamma_{IR} = 6A_u + 9B_u$), which is the same as that proposed in ref 12 for $BiPO_4$-III with the same space group but different from that proposed in ref 15. Marks at the bottom of Figure 2b show the theoretical frequencies of $SbPO_4$ at 0 GPa, for comparison with experimental data. A tentative assignment of the symmetry of the experimental Raman-active modes in light of our theoretical calculations is provided in Table 2.

Figure 2c shows the theoretical PDCs and PDOS at 0 GPa. Acoustic, Raman- and IR-active branches close to Γ have been distinguished and a large phonon gap is observed between 650 and 920 $cm^{-1}$. In order to understand the vibrational modes of $SbPO_4$ at room pressure, we analyzed the Γ eigenvectors computed from the simulations performed at 0 GPa and the J-ICE[58] visualization software (see the Supporting Information for further information). Out of the 33 optical modes, we can comment first on the shear (or transverse) and compressional (or longitudinal) rigid layer modes, which are low-frequency modes typical of layered compounds. For most layered compounds with tetragonal or hexagonal symmetry, the shear rigid layer mode is an $E_g$ mode (doubly degenerate).[59,60] However, $SbPO_4$ has a monoclinic symmetry where doubly degenerate modes are not allowed. For this reason, two shear rigid layer modes ($B_g$ mode at 75 $cm^{-1}$ and $A_g$ mode at 89 $cm^{-1}$) are observed for $SbPO_4$ (see Figures S1 and S2 in the Supporting Information). On the other hand, the $A_g$ mode at 106 $cm^{-1}$ found for $SbPO_4$ is attributed to the compressional rigid layer mode, despite it not being possible to observe a complete movement of one layer against the other (see Figure S3 in the Supporting Information). In the shear rigid layer modes, the atomic vibrations are mainly along the different axis containing the layers (*b* and *c* axes for $SbPO_4$), whereas for the compressional rigid layer mode the atomic vibrations refer to the movement of one layer with the adjacent neighboring layer (Sb atoms against the opposite layer mainly along the *a* axis).

**Table 2. Experimental and Theoretical Raman Mode Frequencies at Zero Pressure and Pressure Coefficients of $SbPO_4$ As Obtained by Fitting the Equation $\omega(P) = \omega_0 + aP$ up to 3 GPa[a]**

| | experimental | | theoretical | |
|---|---|---|---|---|
| symmetry | $\omega_0$ ($cm^{-1}$) | $a$ ($cm^{-1}$/GPa) | $\omega_0$ ($cm^{-1}$) | $a$ ($cm^{-1}$/GPa) |
| $B_g(R)$ | | | 75 | 4.5 |
| $A_g(T)$ | 96 | 0.9 | 89 | 0.5 |
| $A_g(T)$ | 121 | −0.4 | 106 | −0.6 |
| $B_g(R)$ | | | 118 | 5.1 |
| $A_g(T)$ | | | 142 | 2.6 |
| $B_g(T)$ | 152 | 1.7 | 152 | 2.3 |
| $A_g(T)$ | 217 | 0.3 | 200 | 0.6 |
| $B_g(R)$ | | | 224 | 6.1 |
| $A_g(R)$ | 357 | 1.4 | 324 | −1.2 |
| $B_g(\nu_2)$ | | | 347 | −0.8 |
| $A_g(\nu_2)$ | 478 | 3.1 | 452 | 4.4 |
| $B_g(\nu_4)$ | | | 518 | 2.4 |
| $A_g(\nu_4)$ | 584 | −0.5 | 545 | −2.3 |
| $A_g(\nu_4)$ | 623 | 0.9 | 584 | 1.7 |
| $A_g(\nu_1)$ | 937 | 6.0 | 926 | 7.8 |
| $A_g(\nu_3)$ | 977 | 3.6 | 937 | 5.4 |
| $B_g(\nu_3)$ | | | 990 | 0.5 |
| $A_g(\nu_3)$ | 1053 | 4.0 | 1020 | 6.2 |

[a]The notations T, R, $\nu_1$, $\nu_2$, $\nu_3$, and $\nu_4$ refer to the main character of translation, rotation, or internal modes of the $PO_4$ units.

These rigid layer modes are low-frequency modes and are mostly related to the movement of heavy atoms (Sb in $SbPO_4$) as observed in the PDOS below 200 $cm^{-1}$ (see Figure 2c).

It is also worth mentioning that for $SbPO_4$ the internal modes associated with the $PO_4$ tetrahedron are bending and stretching P−O modes located in the medium- and high-frequency regions, respectively (see PDOS in Figure 2c). In fact, as in many phosphates, the vibrational modes of $SbPO_4$ can be understood as internal and external modes of the $PO_4$ units. It is known that the internal modes of the free tetrahedral $PO_4^{3-}$ molecule with $T_d$ symmetry are the symmetric stretching $A_1$ mode (aka $\nu_1$), the triply degenerate $F_2$ asymmetric stretching (aka $\nu_3$), the doubly degenerate E bending mode (aka $\nu_2$); and the triply degenerate $F_2$ bending mode (aka $\nu_4$). These vibrations are located at 938, 1017, 420, and 567 $cm^{-1}$, respectively.[61] In $SbPO_4$, the highest frequency modes (above 900 $cm^{-1}$) are mainly asymmetric stretching modes, except for the symmetrical P−O stretching mode ($A_g$ mode of 936 $cm^{-1}$), in which the four O atoms vibrate in phase against the P atom (see Figure S4 in the Supporting Information). The medium-frequency modes between 400 and 650 $cm^{-1}$ are mostly related to P−O bending: (i) above 540 $cm^{-1}$ these correspond to P−O bending modes combined with Sb−O stretching modes and (ii) below 540 $cm^{-1}$ these correspond to P−O and Sb−O bending modes of both $PO_4$ and $SbO_4$ units. Therefore, we understand that the phonon gap found on $SbPO_4$ is clearly due to the separation of the internal stretching and bending modes evidenced inside the $PO_4$ units.

Finally, the vibrational modes of the low-frequency region below 400 $cm^{-1}$ can be related to translations (T) and rotations (R) of the $PO_4$ units: i.e., the external modes of the $PO_4$ units (see Table 2 and Table S3 in the Supporting Information). In particular, the $A_u$ mode of 220 $cm^{-1}$ corresponds to the rotation of the $PO_4$ units (see Figure S5 in the Supporting Information), and other modes at frequencies between 200 and 330 $cm^{-1}$ also


DOI: 10.1021/acs.inorgchem.9b02268
Inorg. Chem. XXXX, XXX, XXX−XXX

show partial rotation of the $PO_4$ units. It is worth mentioning that the four internal modes of the $PO_4$ units have basically the same frequency of most $APO_4$ compounds due to the strong covalent bond between P and O atoms in comparison to the weaker ionic−covalent $A$−O bonds. This leads us to consider that the $PO_4$ units of most of the $APO_4$ compounds are isolated units stuffed with $A$ cations that lead to a minor perturbation of P−O bonds. The similar frequencies of the internal phonons of the $PO_4$ units of the different phosphates justifies the incompressibility of the $PO_4$ tetrahedron in comparison with other polyhedral units related to the $A$ cation.[19] We would like to point out that, despite the description given above, it is possible to perform more elaborate analyses of the origin of the $SbPO_4$ vibrational modes using, for example, the concept of bond stiffness.[62−64]

**4.2. Structural Properties under Compression.** All XRD peaks shift to larger angles on increasing pressure up to 15.2 GPa, as observed in Figure S6. This result is consistent with the decrease in interplanar distances at increasing pressure. In addition to that, from room pressure up to 8.4 GPa, the only noticeable change on the XRD pattern is the gradual increase of the intensity of the peak at the lowest angle. This phenomenon is the consequence of changes in the coordinates of Sb, which slowly move from the room-pressure position to that of Bi in $BiPO_4$-III, favoring the approximation of Sb to two second-neighboring oxygen atoms, a fact supported by our ab initio simulation. Above 8.4 GPa, we observe the progressive appearance of four additional diffraction peaks (see Figure S6). The new peaks increase in intensity continuously up to the maximum pressure of our XRD study, and these are not related to the monoclinic $SbPO_4$ structure. On pressure release, the obtained diffraction pattern is identical with that of the initial sample, thus showing the reversibility of the pressure-induced PT (see top of Figure S6).

Figure 3 shows the experimental and theoretical pressure dependence of the unit-cell volume of monoclinic $SbPO_4$ up to 14.8 GPa. A third-order Birch−Murnaghan equation of state (BM-EoS)[65] was fitted to our $P$−$V$ data to obtain the zero-pressure volume, $V_0$, bulk modulus, $B_0$, and its pressure derivative, $B_0'$. If the volume vs pressure data are fitted in the whole range, a $B_0'$ value larger than 10 is obtained, thus suggesting an anomalous compressibility behavior. As will be noted below, there is an IPT above 3 GPa. Therefore, we have obtained the EoS at two different pressure ranges: before the IPT (1 atm to 3 GPa) and after the IPT (3−8 GPa). In addition, since the results of the three runs do not present significant divergences, only one adjustment was made on all the experimental points. Both experimental and theoretical data are summarized in Table 3, showing rather good agreement.

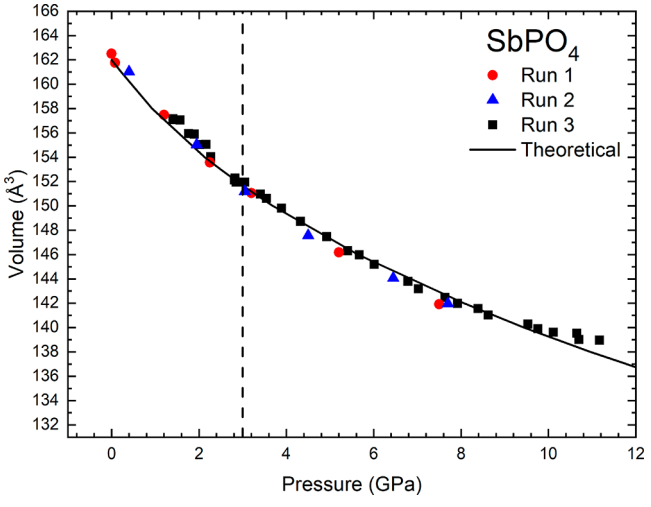


**Figure 3.** Unit cell volume vs pressure for $SbPO_4$. Symbols represent the experimental data, and the solid line represents the theoretical data. The vertical dashed line at 3 GPa indicates the pressure at which the IPT occurs.

As can be noted, when fits are performed from 1 atm to 3 GPa, experimental and theoretical data yield $B_0$ values of 36(3) and 32(1) GPa, respectively. However, after the IPT, both experimental and theoretical data yield a $B_0$ value of 45(2) GPa. The increase in $B_0$ is directly related to an increase in the structure rigidity after the IPT that is common in layered materials.[59,66,67] It is worth mentioning that, with a $B_0$ value of around 34 GPa, $SbPO_4$ is the most compressible phosphate.[18] Interestingly, the bulk modulus of $SbPO_4$ is almost half of that of barite-type compounds, such as $PbSO_4$ and $BaSO_4$,[68−70] and is even smaller than the bulk modulus of the distorted barite-type structure of $SnSO_4$ and respective different layered phases.[71] This is noteworthy because the strong LEP of $Sn^{2+}$ of $SnSO_4$ leads to layered structures with a 3-fold coordinated Sn at the distorted barite-type *Pnma* structure and (3 + 1)-fold coordinated Sn in the $P2_1/a$ phase above 0.2 GPa.[71] Consequently, we can safely conclude that $SbPO_4$ is not only the most compressible phosphate but also one of the most compressible $ABO_4$ compounds.

The pressure dependence of the experimental and theoretical lattice parameters $a$, $b$, $c$, and $\beta$ of monoclinic $SbPO_4$ is shown in Figure 4. The experimental unit-cell parameters as a function of pressure are represented only for $P$ < 11.2 GPa. At higher pressures, phase coexistence does not allow us to obtain them with reasonable accuracy. The axial compressibility, defined as $\kappa_x = -\frac{1}{x}\frac{\partial x}{\partial P}$ ($x$ = $a$, $b$, $c$, $\beta$), obtained from a modified Murnaghan EoS fit to the experimental data[65] is reported in Table 3 and is in good agreement with our theoretical results. As previously, the adjustment was performed for two different pressure ranges: before the IPT (1 atm to 3 GPa) and after the IPT (3−8 GPa). As expected for this layered material, the $a$ axis (direction perpendicular to the layers) presents the largest compressibility due to the high compressibility of the Sb LEP and the weak interlayer Sb−O distances, and the $b$ axis evidenced the lowest value due to the small compressibility of the Sb−O3 and P−O3 bonds mainly directed along this axis. The parameters $a$ and $c$ present a significant decrease in the pressure coefficient at pressures higher than 3 GPa, thus supporting the hypothesis of an IPT around this pressure value. The $\beta$ angle also presents a smooth decrease with pressure and, although our theoretical values present a discrepancy of ∼2° in absolute value with respect to the experimental values, a similar evolution of the experimental and theoretical data with increasing pressure is evidenced. This result indicates that our theoretical data provide a correct description of the evolution of the lattice parameters and $\beta$ angle of the monoclinic structure of $SbPO_4$ under compression.

Since $SbPO_4$ is a monoclinic material, we have calculated and diagonalized the experimental and theoretical isothermal compressibility tensor, $\beta_{ij}$, in order to evaluate the magnitudes and directions of the principal axes of compressibility.[17] The tensor has been calculated using the linear Lagrangian approximation (LLA)[72] and the infinitesimal Lagrangian


DOI: 10.1021/acs.inorgchem.9b02268
Inorg. Chem. XXXX, XXX, XXX−XXX

Table 3. EoS Parameters and Axial Compressibility ($\kappa_x = \frac{-1}{x}\frac{\partial x}{\partial P}$) of $SbPO_4$ before and after the IPT at 3 GPa[a]

| | $V_0$ (Å$^3$) | $B_0$ (GPa) | $B_0'$ | $\kappa_a$ ($10^{-3}$ GPa$^{-1}$) | $\kappa_b$ ($10^{-3}$ GPa$^{-1}$) | $\kappa_c$ ($10^{-3}$ GPa$^{-1}$) | $\kappa_\beta$ ($10^{-3}$ GPa$^{-1}$) |
|---|---|---|---|---|---|---|---|
| experimental | | | | | | | |
| up to 3 GPa | 162.6(6) | 36(3) | 6(2) | 14.6(1) | 5.2(4) | 8.5(6) | 3.8(5) |
| from 3 to 8 GPa | 160.3(8) | 45(2) | 7(3) | 9(1) | 4(1) | 9.7(6) | 1.4(2) |
| theoretical | | | | | | | |
| up to 3 GPa | 163.0(2) | 32(1) | 9(3) | 17.93(4) | 2.7(2) | 14.25(3) | 5.4(1) |
| from 3 to 8 GPa | 160.6(4) | 45(2) | 6(2) | 12.8(2) | 2.9(6) | 11.6(1) | 4.6(15) |

[a]The variation $\frac{\partial x}{\partial P}$ was obtained using the modified Murnaghan equation of state $\Delta x_0/x_0 = (1 + K_{0x}'P/K_{0x})^{-(1/3K_0')} - 1$, where $K_{0x}$ and $K_{0x}'$ are the bulk modulus and its pressure derivative of the $x$ axis ($x = a, b, c, \beta$) at atmospheric pressure, respectively.

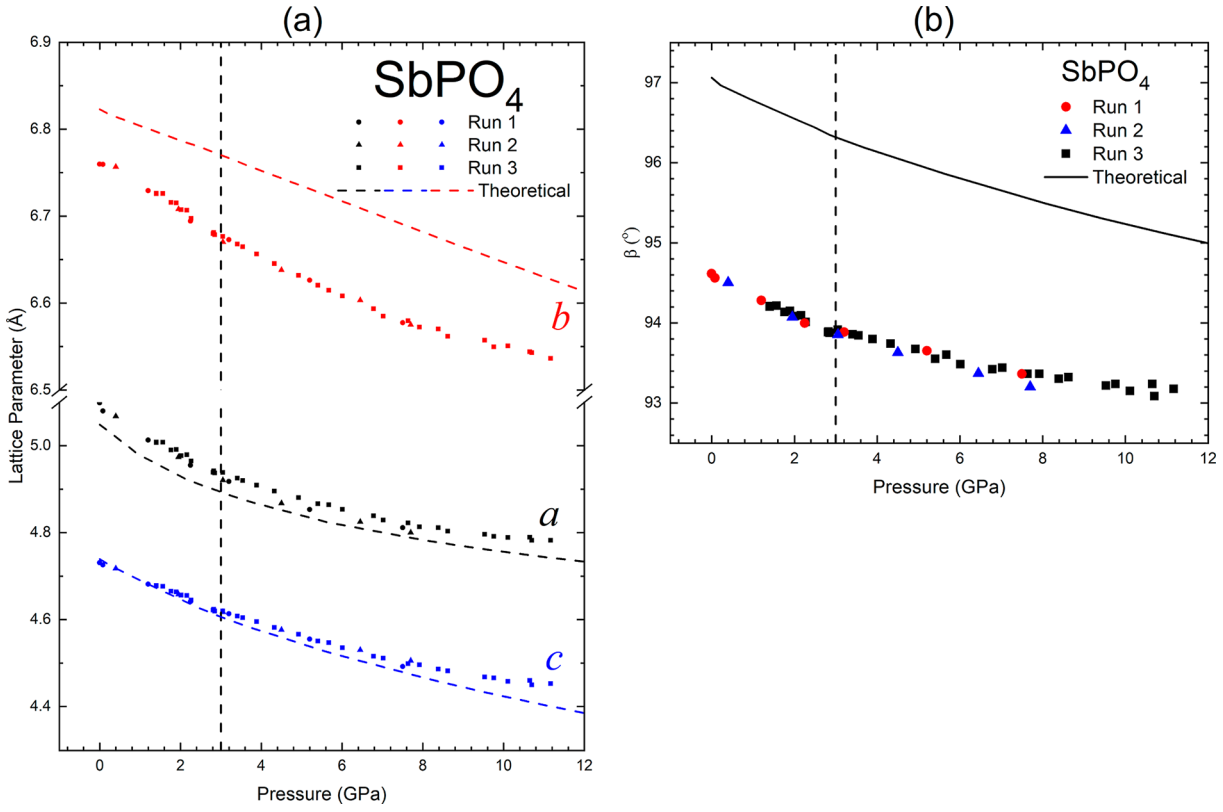


Figure 4. Experimental (symbols) and theoretical (lines) pressure dependence of (a) the lattice parameters $a$, $b$, and $c$ and (b) $\beta$ angle. The vertical dashed lines at 3 GPa indicate the pressure at which the IPT occurs.

approximation (ILA).[73] For the LLA, a linear fit of the unit-cell parameters was carried out in the pressure range 0−5 GPa. Table 4 summarizes the $\beta_{ij}$ coefficients of the isothermal compressibility tensor at zero pressure. It can be observed that there is a qualitative agreement between experimental and calculated data. In addition, the $\beta_{ij}$ coefficients obtained with LLA and ILA are also similar. Notice that $\beta_{22}$ is much smaller than $\beta_{11}$ and $\beta_{33}$, indicating that the $b$ axis is the less compressible axis of $SbPO_4$. On the other hand, from the experiments we obtain that $\beta_{11} > \beta_{33}$, but the opposite result is obtained from calculations. This is caused by the differences in the compressibility of the $a$ axis ($c$ axis), which is slightly underestimated (overestimated) by calculations.

Considering the eigenvalues obtained from experiments using LLA, we obtain that the maximum, intermediate, and minimum compressibilities are $10.22(6) \times 10^3$, $6.18(4) \times 10^3$, and $4.18(2) \times 10^3$ GPa$^{-1}$. Similar results are obtained from other approximations, as can be seen in Table 4. These values are considerably larger than in $BiPO_4$ and $BiSbO_4$,[17,74] which is consistent with the layered structure of $SbPO_4$. The inverse trace of the compressibility tensor, expected to be equal to the bulk modulus, is 48 GPa, which agrees with the result obtained from the BM-EoS.

The eigenvalues and eigenvectors computed for the isothermal compressibility tensor are also reported in Table 4. Considering the eigenvector $ev_2$, the minor compression direction is along the $b$ axis. On the other hand, the major compression direction occurs along the (010) plane at the given angle Ψ (see Table 4) to the $c$ axis (from $c$ to $a$). The direction of maximum compressibility, considering the value of the $\beta$ angle, is at 30(4)° (42°) to the $a$ axis for the case of our experiments (calculations). The direction of intermediate compressibility is also at the same plane, but it is perpendicular to the direction of maximum compressibility. Graphically, the directions of both maximum and intermediate compressibility at room pressure can be observed in Figure S7 in the Supporting Information.


DOI: 10.1021/acs.inorgchem.9b02268
Inorg. Chem. XXXX, XXX, XXX−XXX

**Table 4. Isothermal Compressibility Tensor Coefficients, $\beta_{ij}$, and Their Eigenvalues, $\lambda_i$, and Eigenvectors, $ev_i$, for $SbPO_4$ at Room Pressure**[a]

| | method | | | |
|---|---|---|---|---|
| | linear Lagrangian | | infinitesimal Lagrangian | |
| | experiment | theory | experiment | theory |
| $\beta_{11}$ ($10^{-3}$ $GPa^{-1}$) | 8.99(4) | 8.02 | 10.71(5) | 8.43 |
| $\beta_{22}$ ($10^{-3}$ $GPa^{-1}$) | 4.18(2) | 3.76 | 4.96(2) | 3.85 |
| $\beta_{33}$ ($10^{-3}$ $GPa^{-1}$) | 7.41(4) | 8.62 | 8.75(4) | 8.84 |
| $\beta_{13}$ ($10^{-3}$ $GPa^{-1}$) | −1.86(1) | −2.12 | −2.17(1) | −2.31 |
| $\lambda_1$ ($10^{-3}$ $GPa^{-1}$) | 10.22(6) | 10.47 | 12.11(6) | 10.96 |
| $ev_1$ ($\lambda_1$) | (0.834, 0, −0.557) | (0.655, 0, −0.755) | (0.840, 0, −0.542) | (0.675, 0, −0.738) |
| $\lambda_2$ ($10^{-3}$ $GPa^{-1}$) | 4.18(2) | 3.76 | 4.96(2) | 3.85 |
| $ev_2$ ($\lambda_2$) | (0, 1, 0) | (0, 1, 0) | (0, 1, 0) | (0, 1, 0) |
| $\lambda_3$ ($10^{-3}$ $GPa^{-1}$) | 6.18(4) | 6.17 | 7.35(4) | 6.33 |
| $ev_3$ ($\lambda_3$) | (−0.557, 0, 0.834) | (0.755, 0, 0.655) | (−0.542, 0, 0.840) | (0.738, 0, 0.675) |
| Ψ (deg) | 123(4) | 139 | 123(4) | 137 |

[a]The results are given using the linear Lagrangian and the infinitesimal Lagrangian methods with data from our experiments and our ab initio simulations.

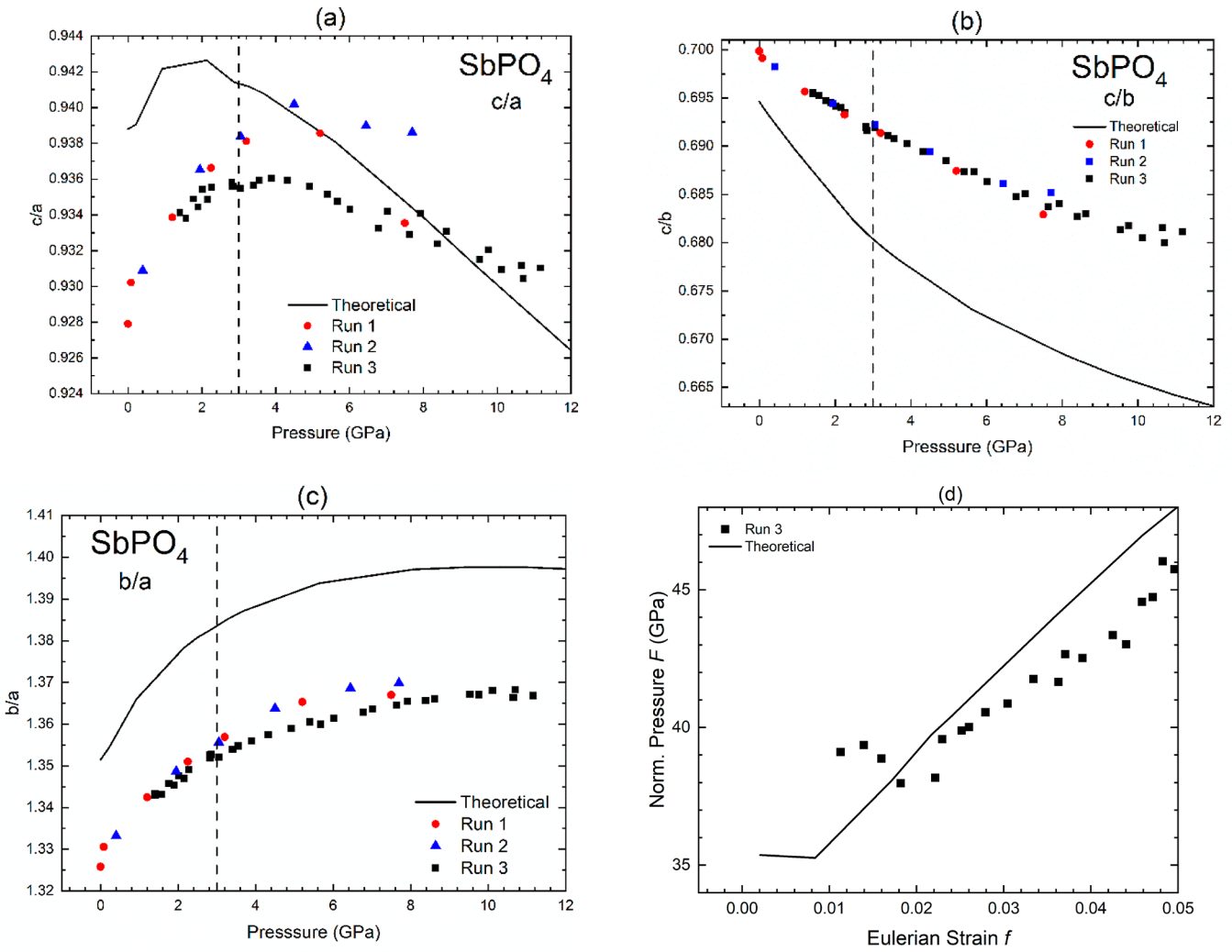


**Figure 5.** Experimental (symbols) and theoretical (lines) pressure dependence of (a) $c/a$, (b) $c/b$, and (c) $b/a$ ratios and (d) normalized pressure vs Eulerian strain plot. The vertical dashed lines at 3 GPa indicate the pressure at which the IPT occurs, as suggested by the change in the pressure coefficients of the axial ratios. Only experimental data of run 3 have been used for the normalized pressure vs Eulerian strain plot due to the extreme sensitivity of this plot to data dispersion.

Using the results of the experimental and theoretical lattice parameters, we have plotted the pressure dependence of the $c/a$, $c/b$, and $a/b$ axial ratios (Figure 5a–c). The results evidence a good agreement of the trends of the experimental and



DOI: 10.1021/acs.inorgchem.9b02268
Inorg. Chem. XXXX, XXX, XXX−XXX

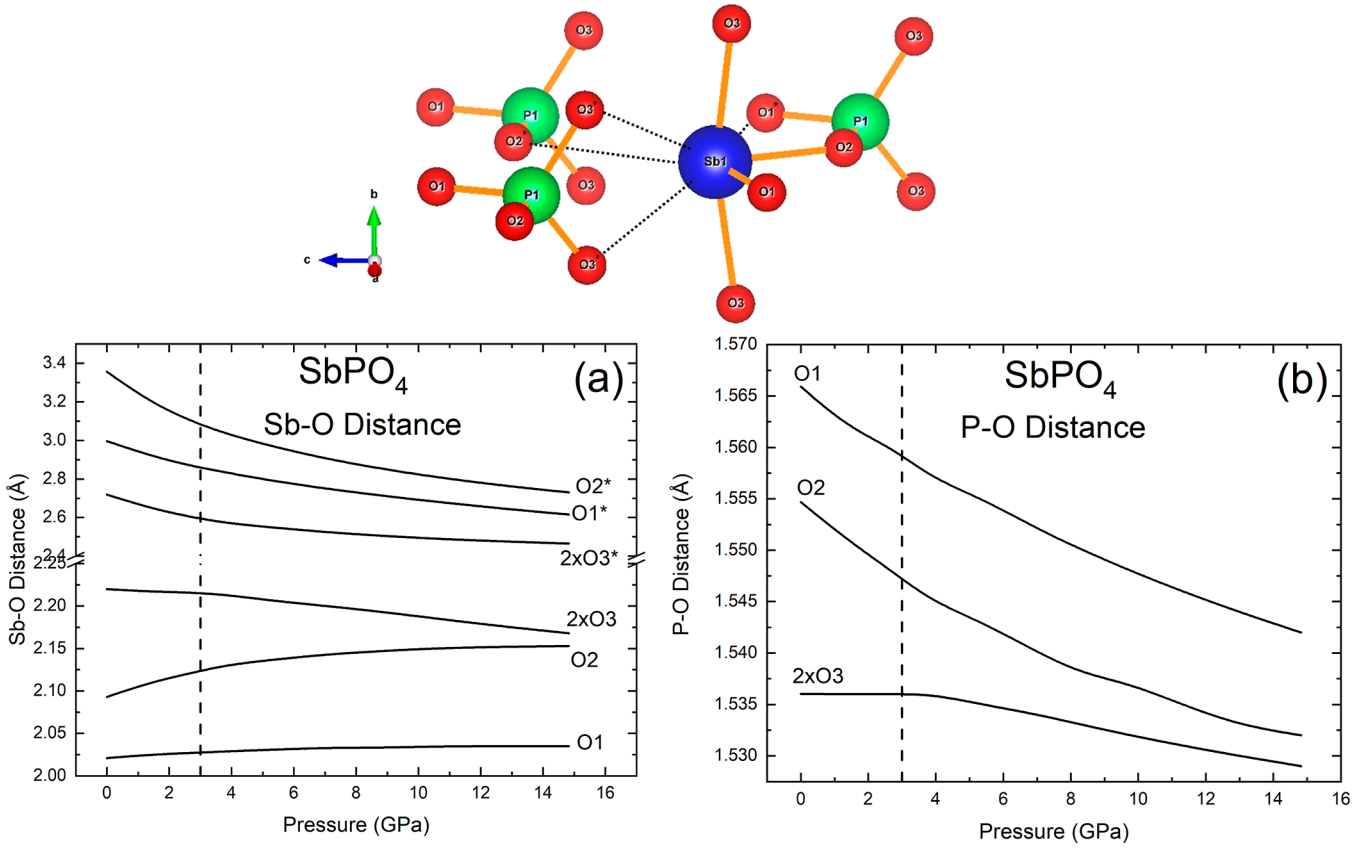


**Figure 6.** Evolution of cation−anion distances of $SbPO_4$ with pressure increase. The asterisks indicate the oxygen distances of an adjacent layer. The results were obtained by theoretical calculations. The vertical dashed lines at 3 GPa indicate the pressure at which the IPT occurs, as suggested by the change of most pressure coefficients of the interatomic distances.

theoretical axial ratios with pressure. The $c/b$ parameter only presents a smooth decrease at HP. On the other hand, the $c/a$ and $b/a$ ratios show a significant increase up to ∼2 and ∼3 GPa, respectively. At higher pressures, the $c/a$ parameter decreases and the $b/a$ tends to stabilize. In Figure 5d we plot the normalized pressure vs eulerian strain plot. As can be observed, both experimental and theoretical $F-f$ data show a change in slope at Eulerian strain values at ∼0.02 (∼3 GPa) and 0.009 (∼2 GPa), respectively. The strong change observed in the slopes of the $c/a$ and $b/a$ axial ratios and the $F-f$ plot above 3 GPa seem to suggest an IPT at around that pressure range, which will be further discussed.

Considering the good correlation between our experimental and theoretical results for monoclinic $SbPO_4$, we can use the theoretical results to extract additional information that is not available through the LeBail fit, such as the evolution of the free atomic positions, bond lengths, and polyhedral distortion at HP. In Figure 6, we can observe the pressure dependence of the theoretical Sb−O and P−O bond lengths. As can be noted in Figure 6a, the shortest Sb−O1 bond length shows no significant change with pressure, but the shortest Sb−O2 and Sb−O3 bond lengths (see solid lines in Figure 1b) tend to converge to the same value as the pressure increases. In this context, it is worth mentioning the increase of the Sb−O2 bond length between 0 and 3 GPa and its change of slope above 3 GPa. Similar changes in slope close to 3 GPa can also be observed at other Sb−O distances. With regard to the largest Sb−O lengths (marked with asterisks in Figure 6a), which correspond to the two interlayer Sb−O3 distances and the two dashed lines shown in Figure 1b, these show a considerable decrease below 3 GPa. Above this pressure value, this tendency decreases but is still reminiscent. Similarly, all P−O bond lengths (Figure 6b) decrease with pressure, except the P−O3 bond, which remains almost constant below 3 GPa and decreases above this pressure.

As already commented, changes in the slopes for the many bond lengths of the monoclinic $SbPO_4$ are observed around 3−4 GPa, especially for distances related to the O3 atom, i.e. the external O atoms of the layers, while smaller changes are associated with O1 and O2 atoms and the internal O atoms of the layers (see Figure 1a,b). To trace the origin of those changes we have plotted in Figure S8 in the Supporting Information the pressure dependence of the Wyckoff sites of monoclinic $SbPO_4$. In order to ensure a good agreement between our theoretical and experimental data, the experimental values obtained by Rietveld refinement at room pressure are also included in Figure S8. As can be observed, the $z$ value of all sites tends to decrease with pressure, except for Sb. It is also possible to observe that the evolution of all positions presents a minor change in the slope around 3 GPa; however, the largest variation in the slope is observed for the $x$ positions of both O2 and O3 and the $y$ position of O3 (Figure S8d,e). These trend variations are indicative of a pressure-induced IPT close to 3 GPa, as previously commented. Further discussion about the IPT will be provided when we discuss the behavior of the electron topology at HP.

In order to find the origin of the new peaks above 8.4 GPa, we provide an indexation of the XRD pattern above that pressure, assuming the possibility of a phase coexistence between the LP phase and a new HP phase or assuming a single HP phase. To search for possible HP structures of $ABO_4$


DOI: 10.1021/acs.inorgchem.9b02268
Inorg. Chem. XXXX, XXX, XXX−XXX

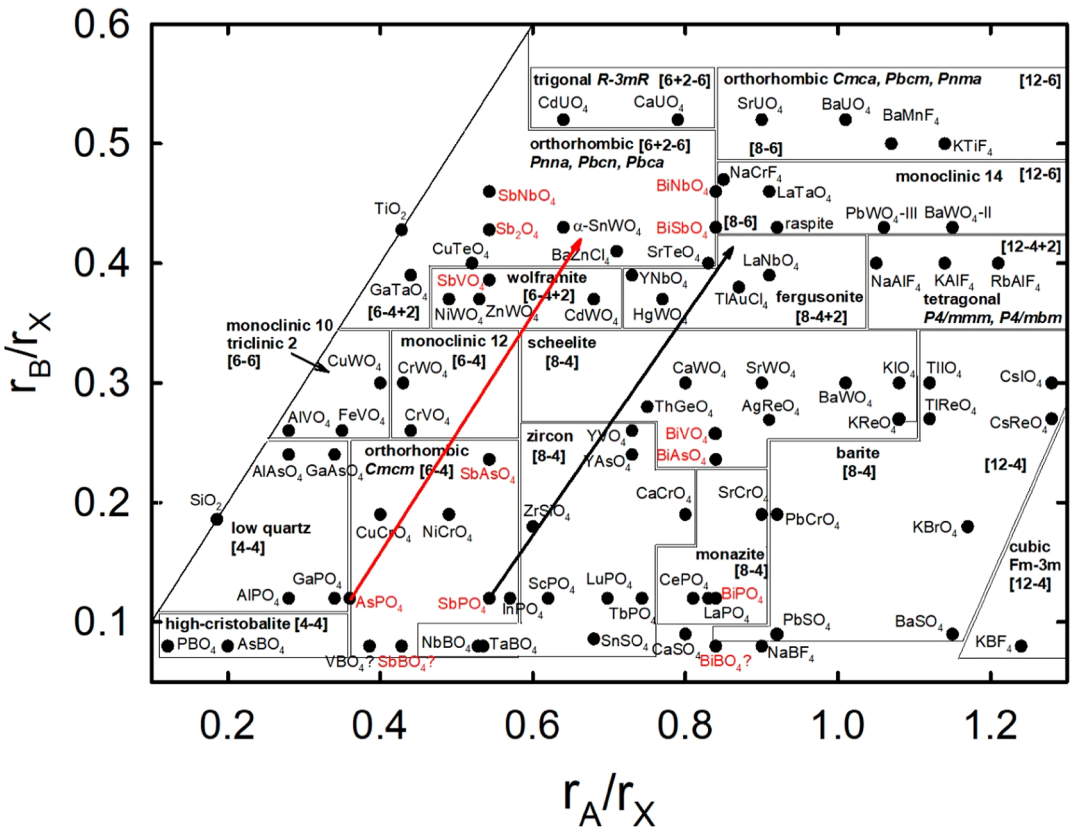


**Figure 7.** Bastide diagram for $ABO_4$ compounds, including the new family of borates and all known compounds containing As, Sb, and Bi with valence 3+.

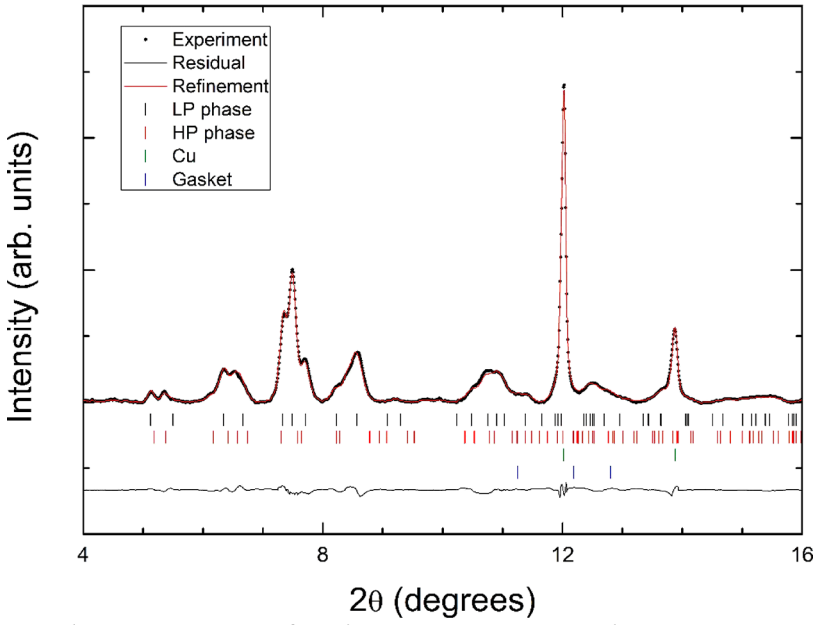


**Figure 8.** Angle-dispersive XRD of $SbPO_4$ measured at 15.2 GPa at room temperature. Experiments, refinements, and residuals are shown. The ticks indicate the position of the peaks of different phases.

compounds, we resorted to a Bastide diagram[20,32] by taking into account the position of $SbPO_4$ in that diagram ($r_{Sb}/r_O$ = 0.563, $r_P/r_O$ = 0.126). We have plotted a renewed form of the Bastide diagram in Figure 7, highlighting the location of many compounds containing cations with LEPs, such as $As^{3+}$, $Sb^{3+}$, and $Bi^{3+}$, which have been positioned in the respective diagram for the first time. We must stress that there are many compounds with $As^{5+}$ in the diagram, with $As^{5+}$ behaving similarly to $P^{5+}$, but there is only one compound of $As^{3+}$ (in red), which is precisely $AsPO_4$ with $P^{5+}$. We must also stress that there are many compounds with $P^{5+}$ in the diagram, but no compound with $P^{3+}$ is mentioned.


DOI: 10.1021/acs.inorgchem.9b02268
Inorg. Chem. XXXX, XXX, XXX−XXX

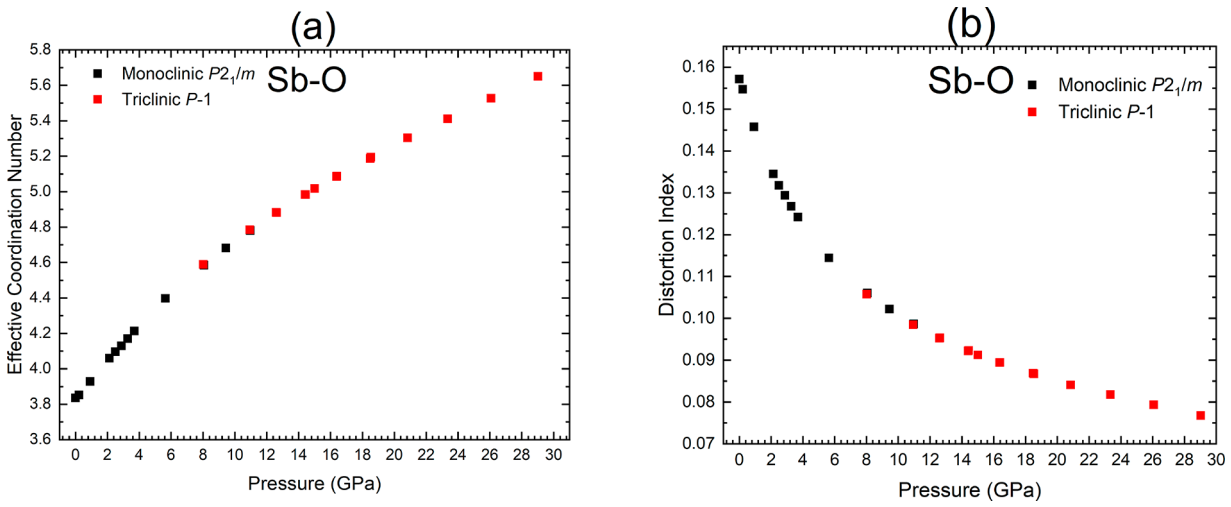


**Figure 9.** Pressure dependence of the (a) effective coordination number (ECoN) and (b) distortion index of the $Sb^{3+}$ of the monoclinic (black squares) and triclinic (red squares) structures of $SbPO_4$ as obtained from our theoretical calculations using the VESTA software.

According to the northeast rule in the Bastide diagram, $SbPO_4$ should crystallize in the orthorhombic $CrVO_4$-type structure with [6-4] coordination for the [*A*-*B*] cations. Moreover, this compound should transform into a zircon or scheelite phase under compression (see black arrow in Figure 7). However, neither of these structures allow us to explain the new peaks observed in Figure S6. Since $BiPO_4$-III transforms into the monazite structure above 0.8 GPa,[12] we have also tried the comparison of the peaks with the monazite structure. However, the position of the new diffraction peaks cannot be explained with a possible PT to this structure either, despite the monazite structure being energetically more favorable than the monoclinic structure at HP.

Since Sb is 4-fold coordinated for the monoclinic structure instead of 6-fold coordinated, as expected from the $Sb^{3+}$ ionic radius, we have considered that the real position of $SbPO_4$ could be that of $AsPO_4$, which is predicted to have 4-fold coordination for As, despite a real 3-fold coordination of As existing at room pressure.[75] In such a case, monoclinic $SbPO_4$ could transform under pressure into the $CrVO_4$ or wolframite structures (see red arrow in Figure 7); however, the positions of the new diffraction peaks cannot be explained with a possible PT to these structures either. Other candidate structures for the HP phase of $SbPO_4$ were also considered: $TiPO_4$, $BaSO_4$, $HgSO_4$, $AgMnO_4$, $BaWO_4$-II, $BiSbO_4$, and the different structures of $SnSO_4$. Note that the $Sn^{2+}$ of $SnSO_4$ also features a strong LEP that leads to the crystallization of $SnSO_4$ in a distorted barite structure. In this context, several compounds featuring other cations with strong LEPs, such as $Sn^{2+}$ and $Pb^{2+}$, are also shown in Figure 7. None of these structures (by themselves or coexisting with the LP phase) enable us to clarify all the Bragg peaks observed for $SbPO_4$ above 8.4 GPa.

Finally, we found a possible solution by considering the coexistence of the LP monoclinic phase of $SbPO_4$ with a respective triclinic distortion. Such coexistence has been observed in other monoclinic oxides at HP.[71,76] In our case, we have built the candidate triclinic structure, which belongs to the $P\bar{1}$ (No. 2) space group, by using the group−subgroup relationships between space groups No. 2 and 11. By considering the coexistence of the LP monoclinic structure and the HP triclinic structure, we have been able to clarify the diffraction patterns measured above 8.4 GPa. Our XRD patterns suggest that the LP phase is the dominant phase up to 11.2 GPa, the HP phase being the dominant phase above this pressure value. In Figure 8, we show the result of the profile matching of the XRD pattern at 15.2 GPa by fixing the atomic coordinates of both monoclinic and triclinic phases to the calculated coordinates at that pressure range. The small residual of the fit supports the hypothesis that the triclinic HP phase is a distortion of the monoclinic LP phase. The *R* values of the fit shown in Figure 8 are $R_p$ = 6.5% and $R_{wP}$ = 8.5%. At 15.2 GPa, the unit-cell parameters of the monoclinic LP phase are $a$ = 4.764(8) Å, $b$ = 6.502(9) Å, $c$ = 4.423(8) Å, and $\beta$ = 92.93(9)°, with $V_0$ = 136.8(7) Å$^3$, while the unit-cell parameters of the triclinic HP phase are $a$ = 4.704(8) Å, $b$ = 6.443(9) Å, $c$ = 4.531(8) Å, $\alpha$ = 92.85(9)°, $\beta$ = 92.93(9)°, and $\gamma$ = 92.47(9)°, with $V_0$ = 136.8(8) Å$^3$. As observed, the volumes of both LP and HP phases at this pressure range are similar, the experimental values of the triclinic HP phase being close to those calculated at 15.0 GPa (see Table S2). This result and the group−subgroup relationship between both structures suggest that the PT could be a very weak first-order transformation, as suggested by the coexistence of both monoclinic and triclinic structures at HP and the reversibility of the XRD pattern at room pressure previously mentioned.

Support for the monoclinic to triclinic PT stems from results obtained from enthalpy vs pressure calculations for both phases which evidence a PT at pressure values of ∼10 GPa (see Figure S9 in the Supporting Information). Nevertheless, there is a possibility that the PT (structural distortion) could be triggered by nonhydrostatic effects.[77] This fact deserves to be studied in the future by further experiments using a selection of different pressure-transmitting media. It must also be stressed that we have found other triclinic structures with lower energy values in comparison to the triclinic structure proposed as the HP phase for $SbPO_4$. These other triclinic structures are the HP structure of $SnSO_4$ observed above 13.5 GPa.[71] However, our XRD patterns at 15.2 GPa cannot be fitted to such structures. Note that these triclinic structures of $SnSO_4$ feature a double unit cell with twice the number of atoms per unit cell in comparison to in our triclinic phase. This would lead to a much larger number of vibrational modes in comparison to those observed above 9 GPa, so we may safely disregard such structures, as we will show in the following section.


DOI: 10.1021/acs.inorgchem.9b02268
*Inorg. Chem.* XXXX, XXX, XXX−XXX

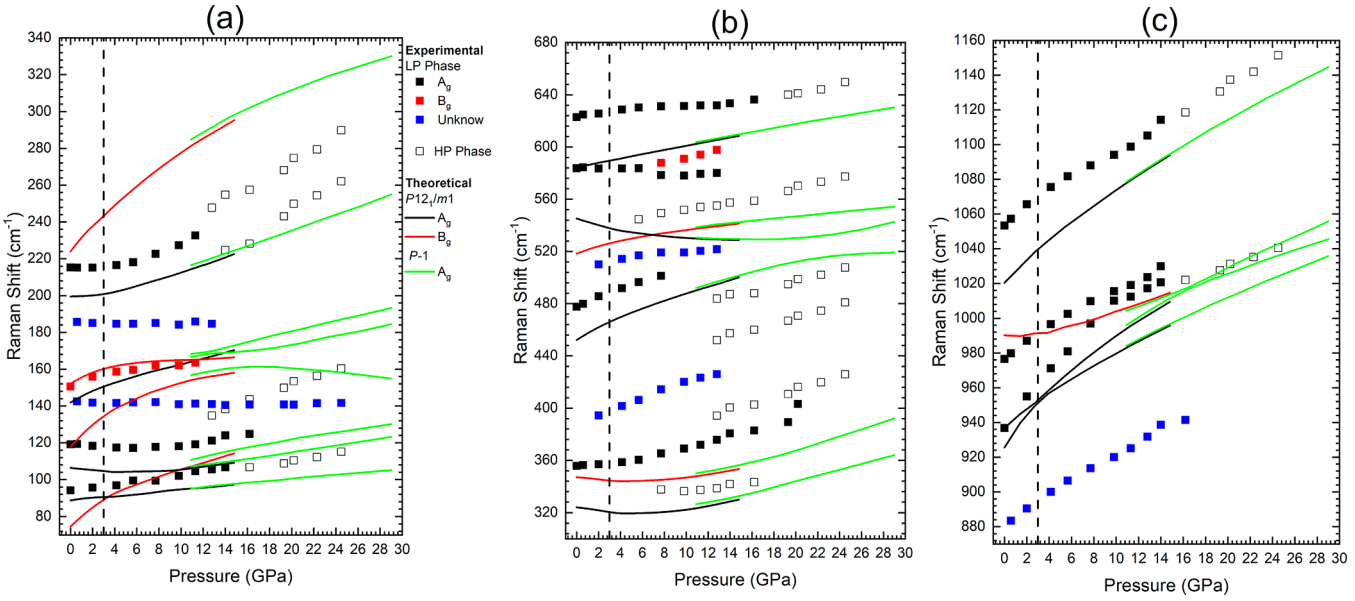


**Figure 10.** Experimental (black, $A_g$; red, $B_g$) and theoretical (lines) pressure dependence of the Raman-active modes of $SbPO_4$: (a) from 75 to 300 cm$^{-1}$; (b) from 300 to 750 cm$^{-1}$; (c) from 870 to 1190 cm$^{-1}$. Lines with different colors represent Raman-active modes of different symmetries. Open symbols represent the new peaks not related to the initial phase. Blue symbols represent the peaks that are not related to the initial $SbPO_4$ phase. The vertical dashed lines at 3 GPa indicate the pressure at which the IPT occur,s as suggested by the change in many frequency pressure coefficients.

Finally, we used the VESTA software[78] in order to evaluate the effective coordination number (ECoN)[79,80] of the Sb and the distortion index[81] of Sb polyhedra in the $P2_1/m$ and $P\bar{1}$ phases of $SbPO_4$ at different pressures (Figure 9). The ECoN scheme has been recently discussed by Guńka and Zachara and shown to be very helpful in discussing the coordination of cations with LEP activity.[82] For this purpose, the pressure dependence of the Sb−O interatomic distances of the eight next-neighboring O atp,s closest to Sb has been obtained from the calculated structures at different pressures. As can be observed in Figure 8a, the Sb ECoN of the LP phase of $SbPO_4$ (3.83 at 0 GPa) is consistent with the 4-fold coordination of Sb at room pressure. The ECoN increases steadily with pressure in the LP phase and reaches 4.78 at 10.97 GPa, thus pointing to a (4 + 2)-fold coordination of Sb at this pressure, since there are two additional Sb−O3 interlayer distances with the same length. Above this pressure, the HP phase becomes more stable and the evolution of the ECoN of Sb of the HP phase presents the same growth rate as that of the LP phase, thus reaching an ECoN of 5.19 at 18.5 GPa. We will see later that this value is consistent with a (4 + 2 + 1)-fold coordination for Sb coordination for this pressure range. The increase of ECoN with pressure is followed by the decrease in the distortion index (Figure 9b) that above 4.7 GPa presents a decrease in the distortion rate and remains constant in the HP phase. Moreover, the increase in the Sb coordination in the monoclinic phase from 4 to 4 + 2 can be related to the strong decrease in the Sb eccentricity of the $SbO_6$ polyhedra between 1 atm and (see Figure S10).

Finally, we must stress that the ECoN value of Sb in $SbPO_4$ at 18.5 GPa is close to that of Bi for $BiPO_4$-III at room pressure (5.16); therefore, we can conclude that around 18 GPa the $SbPO_4$ compound behaves like $BiPO_4$-III at room pressure.[19] In other words, pressure promotes the approach of the layers in $SbPO_4$, thus favoring the bond between the $Sb^{3+}$ of one layer and the $O^{2-}$ atoms of the adjacent layer, therefore converting the 2D-type structure of $SbPO_4$ at room pressure into a 3D-type structure that reaches a coordination similar to that of $BiPO_4$-III at pressures close to 18 GPa.

We conclude by mentioning that the proposed pressure-induced IPT at 3 GPa and monoclinic−triclinic PT above 9 GPa does not involve a change in the coordination of P, although a considerable increase of the coordination of Sb from 4 at room pressure to 4 + 2 above 3 GPa is observed; moreover, the respective coordination increases to 4 + 2 + 2 above 9 GPa (see Figure 1c). In fact, we may consider the IPT at 3 GPa as being the onset of a 2D to 3D PT due to the increase of coordination to 4 + 2 caused by two new Sb−O3 interlayer bonds. This can be seen as a gradual distortion of the crystal structure favored by the presence of a LEP, which gives a large flexibility to the crystal structure to accommodate stresses/strain. It is a phenomenon analogous to what we have seen in $CuWO_4$,[83] where there is a pressure-induced structural distortion in order to preserve the Jahn−Teller distortion of the compound. On the other hand, the coordination of Bi of the $BiPO_4$-III structure at 0 GPa is practically 6, which explains why this material does not form layers at room pressure, unlike $SbPO_4$, and why $BiPO_4$-III varies directly to coordination 6 + 2 at HP (in the monazite phase).[19]

### 4.3. Vibrational Properties under Compression.

Raman scattering (RS) spectra at selected pressures up to 24.5 GPa are presented in Figure S11. Once the sample is inside the pressure cell, it is possible to observe some peaks that probably are not related to the $SbPO_4$ sample (see blue arrows in Figure S11), since these do not appear on the RS spectra at room pressure either before or after the HP cycle (see bottom and top RS spectra in Figure S11). These peaks could be due to some unintentional impurity loaded on the DAC. The pressure dependence of these peaks is plotted as blue symbols in Figure 10, and some of them can be observed up to the maximum pressure of our RS experiment.


DOI: 10.1021/acs.inorgchem.9b02268
Inorg. Chem. XXXX, XXX, XXX−XXX

With regard to the peaks that may be considered as first-order modes of $SbPO_4$, some of these begin to widen and lose intensity and other new peaks start to rise above 7.7 GPa (see red arrows in Figure S11a–c), thus giving support to the existence of a PT above this pressure range. In particular, the peak that rises at 12.8 GPa around 134.7 $cm^{-1}$ and at 24.5 GPa around 160.4 $cm^{-1}$ (Figure S11a) becomes the most intense peak of the RS spectrum of the HP phase. Seven other less intense new peaks can be observed in the pressure range of 7.7 to 16.2 GPa. Notably, the peaks initially observed at 355 $cm^{-1}$ (the strongest peak of the LP phase) and at 888 $cm^{-1}$ (probable second-order mode of the LP phase) progressively disappear with increasing pressure, thus indicating that the PT seems to be complete around 20 GPa. This result could explain why our XRD measurements up to 15 GPa cannot clearly resolve the HP phase, since this phase is not completely developed at this pressure range. Note also that the region which presents fewer changes in the Raman spectrum is the high-frequency region related to the stretching P–O vibrations of the $PO_4$ unit. This means that the HP phase is most likely to be a phase with tetrahedral coordination of P, in good agreement with the proposed triclinic HP phase and with the higher pressure phase at which the P coordination has been observed to increase on other phosphates.[30,84]

Figure 10 presents the dependence of the experimental and theoretical frequencies of the Raman peaks of $SbPO_4$ at HP, which is also summarized in Table 2. For the sake of completeness, we also plotted the dependence of the theoretical IR-active modes at HP in Figure S12in the Supporting Information, whose data are summarized in Table S3 in the Supporting Information. Comparing the evolution of the theoretical and experimental results at HP, we can note that results obtained from ab initio calculations underestimate the frequencies of all Raman-active modes. This underestimation (typically within 3–5%) is especially evident in the medium- and high-frequency regions, where frequency values differ up to 30 $cm^{-1}$. However, comparing the pressure evolution of both data, we can tentatively assign the symmetry irreducible representations of some experimental Raman-active modes with the aid of theoretical calculations (see Table 2 and Figure 10). For this purpose, we have calculated the pressure coefficients of the Raman peaks up to 3 GPa (Table 2) due to the IPT observed above 3 GPa. Curiously, all experimentally observed peaks at room pressure can be associated with the $A_g$ modes, except for the peak located at 151 $cm^{-1}$, which we attribute to the $B_g$ mode at 151 $cm^{-1}$. Finally, it must be mentioned that the signature of the experimental broad peak initially observed at 107 $cm^{-1}$ is not clear, since it was observed only at 1 atm outside the DAC (before and after the pressure cycle).

As can be observed in Figure 10, many vibrational modes present a change in the pressure coefficient between 3 and 6 GPa, reinforcing the idea of the existence of a pressure-induced IPT around 3 GPa. In particular, experimental Raman-active modes Ag(T) (near 215 $cm^{-1}$) and Ag(R) (near 356 $cm^{-1}$) as well as a number of theoretical Raman-active modes (at 75, 106, 118, 152, 200, 324, 347, and 990 $cm^{-1}$ at 0 GPa in Table 2) show a change of slope close to 3 GPa in Figure 9. Moreover, all the vibrational modes of $SbPO_4$ that show a negative pressure coefficient at 0 GPa change to a positive pressure coefficient above 3 GPa. This result is in good agreement with the pressure-induced 2D to 3D phase transition that takes place in layered $SbPO_4$ above 3 GPa upon increasing Sb coordination from 4- to (4 + 2)-fold. On the other hand, the nonlinear behavior of the theoretical vibrational modes located at 926 and 937 $cm^{-1}$ at room pressure is the result of an anticrossing of these two $A_g$ modes, which is reproduced by the experimental results at a slightly higher pressure value (~12 GPa; Figure 10c). A change in pressure coefficient around 3 GPa can also be observed for many theoretical IR-active modes (Figure S12), where a couple of anticrossings seem also to be observed for the $B_u$ peaks at 183 and 207 $cm^{-1}$ (Figure S12a) and at 930 and 937 $cm^{-1}$ (Figure S12c), respectively. The change in the pressure coefficient of the Raman-active and IR-active modes near 3 GPa can be related to the approximation of the atomic layers that begin to interact more strongly and lead to the increase in Sb coordination. Note that the compression of the LEP is much larger than that of other bonds, thus leading to a large compression of the interlayer distance below 3 GPa (compression is less pronounced at higher pressures).

At this point, we can discuss the pressure coefficients of the vibrational modes. It can be observed that the largest pressure coefficients correspond mostly to the P–O vibrations stretching located at the high-frequency region. In particular, the highest-pressure coefficient is that of the symmetric stretching $A_g$ mode and the respective IR analogue, the $B_u$ mode. A similar high response to pressure of the stretching P–O vibrations, and in particular of the symmetric stretching modes, has been found for other orthophosphates.[19,20,26,85−88] Large pressure coefficients are also observed for the rotational modes of the $PO_4$ unit (theoretical $A_u$ and $B_g$ modes at 220 and 224 $cm^{-1}$, respectively). Again, this behavior has already been observed for other orthophosphates.[19,20,26,85−88]

With regard to the rigid layer modes, the shear rigid layer modes positioned at 75 $cm^{-1}$ ($B_g$ mode) and at 89 $cm^{-1}$ ($A_g$ mode) have pressure coefficients of 4.5 and 0.5 $cm^{-1}$/GPa, respectively. On the other hand, the longitudinal rigid layer mode at 106 $cm^{-1}$ ($A_g$ mode) has a pressure coefficient of −0.6 $cm^{-1}$/GPa (see Table 2). For typical layered materials with van der Waals interactions between the layers, such as GaSe and InSe, the longitudinal rigid layer mode has a larger pressure coefficient (above 3 $cm^{-1}$/GPa) in comparison to that of the shear rigid layer mode (between 0.5 and 1.5 $cm^{-1}$/GPa; see discussion in refs 59 and 89). The situation of $SbPO_4$ is completely different from that of typical layered compounds but also different from that of BiTeBr and BiTeI with polar interactions between the layers.[59] On one hand, the lowest-frequency $A_g$ mode is a typical shear rigid layer mode (see Figure S2) and evidences a pressure coefficient below 1 $cm^{-1}$/GPa. On the other hand, the shear rigid layer $B_g$ mode shows an extraordinarily high pressure coefficient. This can be explained by taking into account the atomic vibrations of this latter mode (see Figure S1). It can be observed that the $B_g$ mode is not a pure shear mode because it involves mainly motion of the Sb atom with both Sb and O of the same sublayer vibrating out of phase. Therefore, this mode is a mixture of an asymmetric stretching of Sb–O3 bonds and bending of Sb–O1 and Sb–O2 bonds within the $SbO_4E$ unit, which justifies the high value of the pressure coefficient of this mode.

Finally, we want to highlight that the negative pressure coefficient for the longitudinal rigid layer mode is a characteristic feature of $SbPO_4$ not reported for any other layered compound to our knowledge. A positive pressure coefficient for this mode has been observed in all van der Waals type layered compounds, i.e. InSe and GaSe and other related materials, and also for layered compounds with polar interlayer interaction,


DOI: 10.1021/acs.inorgchem.9b02268
Inorg. Chem. XXXX, XXX, XXX–XXX

Table 5. Experimental and Theoretical Raman Mode Frequencies and Pressure Coefficients of the Triclinic HP Phase ($P\bar{1}$) of $SbPO_4$ Obtained by Fitting the Equation $\omega(P) = \omega_{10.9\,GPa} + aP$ from 10.9 GPa up to 14 GPa

| | experimental | | theoretical | |
|---|---|---|---|---|
| symmetry | $\omega_{10.9\,GPa}$ ($cm^{-1}$) | $a$ ($cm^{-1}$/GPa) | $\omega_{10.9\,GPa}$ ($cm^{-1}$) | $a$ ($cm^{-1}$/GPa) |
| $A_g$ | 106.7 | 1.0 | 95.0 | 0.7 |
| $A_g$ | 134.7 | 2.2 | 107.3 | 0.7 |
| $A_g$ | | | 110.8 | 1.4 |
| $A_g$ | | | 156.8 | 1.1 |
| $A_g$ | | | 166.8 | 0.6 |
| $A_g$ | | | 168.3 | 1.1 |
| $A_g$ | 223.3 | 3.8 | 216.5 | 2.1 |
| $A_g$ | 247.7 | 3.4 | 284.9 | 3.5 |
| $A_g$ | | | 326.6 | 1.5 |
| $A_g$ | 394.2 | 1.9 | 350.1 | 1.6 |
| $A_g$ | 452.0 | 2.4 | 492.1 | 2.4 |
| $A_g$ | 483.8 | 2.0 | 530.6 | −0.3 |
| $A_g$ | 555.2 | 2.0 | 538.6 | 1.0 |
| $A_g$ | 631.7 | 0.5 | 603.7 | 1.5 |
| $A_g$ | 1022.0 | 2.2 | 984.1 | 3.0 |
| $A_g$ | | | 996.1 | 3.9 |
| $A_g$ | | | 1004.3 | 2.4 |
| $A_g$ | 1118.6 | 4.0 | 1078.6 | 4.1 |

such as BiTeBr and BiTeI.[59] The positive value of this pressure coefficient for van der Waals type compounds is related to the increase in the interlayer strength with increasing pressure. A closer look at the atomic vibrations of this mode shows that this mode is also a mixture of an asymmetric stretching of the Sb−O2 bond and bending of Sb−O1 and Sb−O3 bonds within the $SbO_4E$ unit. Therefore, the negative pressure coefficient for this mode in $SbPO_4$ is most likely related to a decrease in the Sb−O2 bond strength, which is in good agreement with the increase in the Sb−O2 bond distance between 0 and 3 GPa (see Figure 6). Note that the change in the pressure coefficients of many vibrational modes is also in agreement with the changes of the Sb−O distances observed in Figure 6, thus providing additional support to the occurrence of a second-order IPT for $SbPO_4$ around 3 GPa.

Several new Raman-active modes (Figure S11) observed above 12.8 GPa have been attributed to the HP phase. Group theoretical considerations for the proposed triclinic ($P\bar{1}$) HP phase yield 36 normal modes of vibration at Γ, whose mechanical decomposition has the form[57]

$$\Gamma = 18A_g(R) + 15A_u(IR) + 3A_u$$

where $A_g$ are Raman-active (R) and $A_u$ are IR-active, except for the three acoustic modes. Therefore, there are 18 Raman-active and 15 IR-active modes. The 18 Raman-active and 15 IR-active theoretical modes have been plotted in Figure 10 and Figure S13, respectively. As observed in Figure 10, the theoretical Raman-active modes for the HP phase of $SbPO_4$ show frequencies and pressure coefficients similar to those of the LP phase. Table 5 summarizes the frequencies and pressure coefficients of the experimental and theoretical modes of the HP triclinic phase of $SbPO_4$. Despite of there not existing a very good agreement between the experimentally measured modes of the HP phase and the calculated mode, we have provided in Table 5 a tentative assignment of the experimental modes to this triclinic phase. The theoretical frequencies and pressure coefficient of the IR-active modes of the proposed triclinic HP phase of $SbPO_4$ are also summarized in Table S4 in the Supporting Information. Regarding the relative disagreement between calculated and experimental triclinic Raman-active modes in Table 5, we think that it can be due to experimental problems of appearance of second-order modes instead of first-order modes of the triclinic phase or to theoretical problems regarding the simulation of the correct triclinic phase, since the experimental triclinic phase could be slightly different from the simulated phase. Regarding this point, we must note that the simulation of triclinic phases is very challenging, since energy minimization procedures can lead to local minima and not to absolute minima. This means that we have found a triclinic phase which is competitive with the monoclinic phase at HP, but we cannot ensure that this is the only triclinic competitive phase and therefore we cannot ensure that the simulated phase is exactly the experimental phase.

In summary, our unpolarized HP-RS measurements of $SbPO_4$ exhibit most of the Raman-active modes of the monoclinic ($P2_1/m$) phase with $A_g$ symmetry but very few modes with $B_g$ symmetry. The assignment of vibrational modes as internal or external of the $PO_4$ units has been provided and their pressure coefficients, especially those for rigid layer modes, have been properly discussed. HP-RS results support the occurrence of an IPT around 3 GPa and a PT above 8 GPa that complete respective formation around 20 GPa, in good agreement with the XRD measurements. Finally, the Raman-active modes of the HP phase of $SbPO_4$ have been measured and their frequencies have been compared to the theoretically predicted modes for the HP triclinic phase.

**4.4. Electronic Properties under Compression.** In order to understand the electronic properties of $SbPO_4$, we have calculated the theoretical electronic band structure of $SbPO_4$. Figure 11 shows the theoretical electronic band structure and PDOS of $SbPO_4$ at 0 and 5.1 GPa. As observed in Figure 11a, $SbPO_4$ presents a calculated indirect band gap of 3.84 eV at 0 GPa, whose valence band maximum (VBM) and conduction band minimum (CBM) are located at the $C_2$ and B points of the BZ, respectively. A second minimum of the conduction band is located at the $Y_2$ point of the BZ. Therefore, on consideration of the underestimation of the band gap from DFT-PBEsol calculations, the real band gap must be well above


DOI: 10.1021/acs.inorgchem.9b02268
Inorg. Chem. XXXX, XXX, XXX−XXX

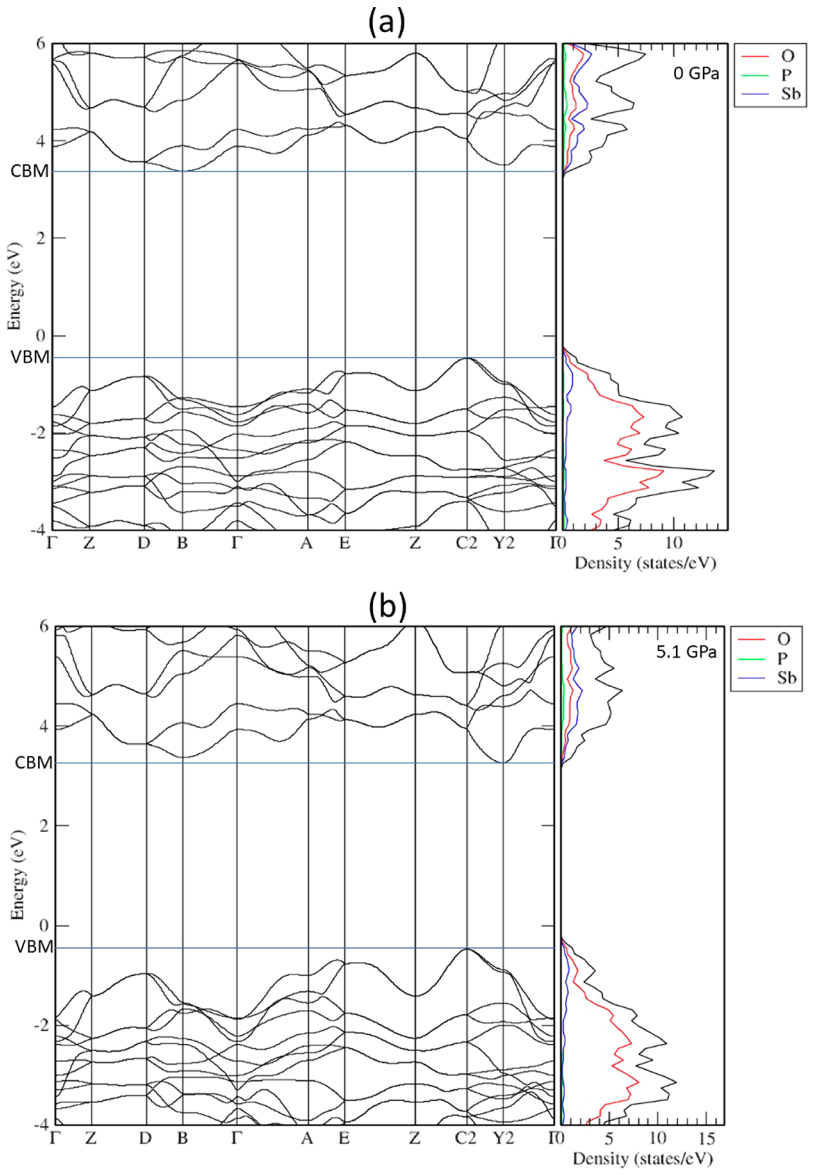


**Figure 11.** Theoretical electronic band structure of monoclinic $SbPO_4$ at (a) 0 GPa and (b) 5.1 GPa. The VBM and CBM lines indicate the valence band maximum and conduction band minimum, respectively.

3.84 eV at room pressure. This means that $SbPO_4$ is an insulating and transparent material in the visible, UVA, and UVB ranges. The maximum of the valence band is dominated by O states while the minimum of the conduction band is dominated by Sb states.

In Figure 11b it is possible to observe that, at 5.1 GPa, the minimum of the conduction band is located at point $Y_2$, indicating that the band gap at this pressure range is measured between the high-symmetry points of $C_2$ and $Y_2$. The pressure dependence of both indirect $C_2$−B and $C_2$−$Y_2$ band gaps is plotted in Figure 12. As can be observed, the indirect $C_2$−B band gap increases with pressure whereas the indirect $C_2$−$Y_2$ band gap decreases with pressure. Consequently, an indirect to indirect crossover in the conduction band minimum occurs around 2.4 GPa: i.e., close to the IPT pressure. Above this pressure, the minimum indirect band gap is found to be between the $C_2$ and $Y_2$ high-symmetry points of the BZ.

To complete the picture of the evolution of $SbPO_4$ under compression and probe the variations of the Sb coordination as a function of pressure, we have performed an analysis of the ELF and the electron charge density using the QTAIM formalism for the different Sb−O bonds at different pressures in both monoclinic and triclinic $SbPO_4$, which can be compared to the ECoN (Figure 9a). The ELF analysis is shown in Figure 13, where some remaining nonsmoothness of the curves is due to the impossibility of raising the number of radial points further. We note that an all-electron wave function is needed to get a reliable picture of the ELF, since this function is not separable into core and valence contributions. The value of the ELF along lines connecting Sb to its O neighbors were calculated by three-dimensional interpolation from the ELF grid generated by Elk using the CRITIC2 software.[49] For the AIM electron density analysis, we have computed the electronic charge density and respective Laplacian at the BCPs also using CRITIC2 software (see Table S5). With this information, we have analyzed the Sb−O interatomic interactions in the different $SbPO_4$ structures in order to study the variation in Sb coordination as a function of pressure. At 0 GPa, Sb is 4-fold coordinated in


DOI: 10.1021/acs.inorgchem.9b02268
Inorg. Chem. XXXX, XXX, XXX−XXX

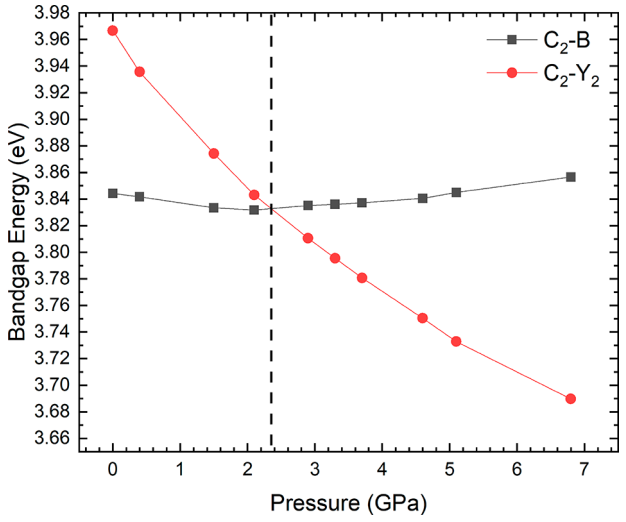


**Figure 12.** Pressure dependence of the theoretical indirect band gaps $C_2-Y_2$ and $C_2-B$ in monoclinic $SbPO_4$ up to 6.8 GPa. The vertical dashed line indicates the pressure at which the crossing of the two indirect band gaps occur.

monoclinic $SbPO_4$ with four Sb−O distances ($d_1$, $d_2$, and two $d_3$) below 2.2 Å (see Figure 6a). All four bonds show a similar ELF profile and a minimum near 0.44 of the normalized distance in Figure 13a and also similar values of the electron density at their BCPs. On the other hand, the remaining four Sb−O distances (two $d_4$, $d_5$, and $d_6$ above 2.7 Å) present completely different ELF profiles that show the existence of a maximum near 0.4 of the normalized distance that corresponds to the Sb LEP and a minimum close to 0.52 for $d_4$, 0.53 for $d_5$, and 0.54 for $d_6$. With regard to the electron density, the $d_4$ and $d_6$ Sb−O distances show charge densities at the corresponding BCPs that are significantly smaller than in the short contacts, and the $d_5$ contact does not even have a BCP (see Table S5). These observations evidence the negligible Sb−O interaction along these directions, which agrees with the ECoN results regarding the 4-fold coordination of Sb for the monoclinic $SbPO_4$ systems at 0 GPa.

Above 3 GPa, monoclinic $SbPO_4$ shows four Sb−O bond lengths ($d_1$ to $d_3$) below 2.2 Å and two Sb−O bonds ($d_4$) below 2.6 Å (see Figure 6a). The four shortest distances show ELF profiles similar to those at 0 GPa, and the other two distances ($d_4$) show an ELF profile where the LEP maximum is almost gone and there is a minimum closer to 0.44; i.e. similar to those of $d_1$ to $d_3$ distances (Figure 13b), thus indicating that the ELF domain associated with the LEP has shrunk. Similarly, at this pressure, the charge density of $d_4$ has increased significantly in comparison to the evolution of the density at the $d_1$, $d_2$, and $d_3$ BCPs. This picture of the ELF and charge density at the BCP is consistent with the (4 + 2)-fold Sb coordination that occurs above the IPT. Moreover, the BCP along the $d_5$ distance appears at pressures above 3 GPa, thus giving support to the occurrence of an IPT above this pressure involving a change from 4-fold to (4 + 2)-fold Sb coordination. Note that at 7.1 GPa the ELF of the $d_5$ and $d_6$ distances still show the LEP maxima near the 0.4 normalized distance (Figure 13b) and the charge densities at the BCPs of these two distances are smaller than the others (see Table S5), thus supporting the (4 + 2)-fold coordination of $SbPO_4$ of the monoclinic phase up until 8 GPa. We also point out that the Laplacian of all BCPs is positive, thus evidencing the ionic character of all Sb−O bonds, regardless of bond distance.

Regarding the triclinic phase, we find four distances below 2.15 Å, two distances below 2.5 Å, and the remaining two distances below 2.7 Å above 8 GPa. At 14.4 GPa, all $d_1$ to $d_8$ distances show ELF profiles (see Figure 13c) similar to those found in monoclinic $SbPO_4$ at 7.1 GPa (see Figure 13b). The degeneracy of bonds $d_3$ and $d_4$ in the monoclinic phase is broken in the triclinic phase; thus, we find $d_1$ to $d_4$ ($d_5$ to $d_6$) distances in the triclinic phase showing ELF profiles similar to those of $d_1$ to $d_3$ ($d_4$) distances in the monoclinic phase. Similarly, $d_7$ and $d_8$ distances in the triclinic phase show ELF profiles similar to those of $d_5$ and $d_6$ in the monoclinic phase. This is consistent with the 4 + 2 coordination of Sb in triclinic $SbPO_4$ at 14.4 GPa.

At 20.8 GPa, the picture is slightly different because the ELF maximum due to the Sb LEP is gone for the $d_7$ distance; i.e., the $d_7$ distance shows an ELF profile similar to that of $d_5$ and $d_6$ distances (see Figure 13d). This suggests an increase of coordination to 4 + 2 + 1 for Sb. This interpretation is in agreement with the fact that the charge density at the BCPs of the $d_7$ distance has values comparable to those in the $d_4$ distance of the monoclinic phase. Moreover, this conclusion is in agreement with the fact that the Sb coordination in $SbPO_4$ reaches the effective coordination found for Bi in $BiPO_4$-III at 0 GPa. Note that the charge density value of the $d_8$ distance is smaller than the others and the ELF profile of the $d_8$ distance still exhibits the maximum of the Sb LEP at 20.8 GPa. We interpret this as indicating that the triclinic structure Sb does not undergo a 4 + 2 + 1 + 1 coordination up to higher pressure (likely above ca. 25 GPa).

In summary, we have demonstrated with the calculated ELFs and the charge densities and respective Laplacians at the BCPs of the shortest Sb−O distances that in $SbPO_4$ (i) a change in the number of BCPs of Sb occurs at the IPT close to 3 GPa and (ii) an increase in Sb coordination can be evidenced by the charge density accumulation at the BCPs and by the disappearance of the Sb LEP maximum of the ELF, supporting the conclusion related to the increase of Sb coordination previously shown by the ECoN.

## 5. CONCLUSIONS

We have reported a joint experimental and theoretical study of the structural and vibrational properties of $SbPO_4$ at HP by means of XRD and RS measurements combined with ab initio calculations. From a structural point of view, we have shown that $SbPO_4$ is one of the most compressible materials (bulk modulus around 20 GPa), not only among phosphates but also among $ABO_4$ compounds. Moreover, its compressibility tensor evidences a considerable anisotropic behavior due to a high nonlinear compression, mainly along the $a$ axis. Additionally, our results have shown that $SbPO_4$ undergoes an IPT around 3 GPa and a PT above 9 GPa, which is complete around 20 GPa.

After the study of several candidates for the HP phase of $SbPO_4$ in light of an updated Bastide diagram containing many $ABO_4$ compounds with strong cation LEPs, we have proposed a triclinic distortion of the original monoclinic phase as the HP phase above 9 GPa. The Raman-active modes of both LP and HP phases have been measured and properly discussed at different pressures. In general, a rather good agreement is observed between the experimental and theoretical data for the structural and vibrational data. Finally, we have provided the electronic band structure of monoclinic $SbPO_4$ at different


DOI: 10.1021/acs.inorgchem.9b02268
Inorg. Chem. XXXX, XXX, XXX−XXX

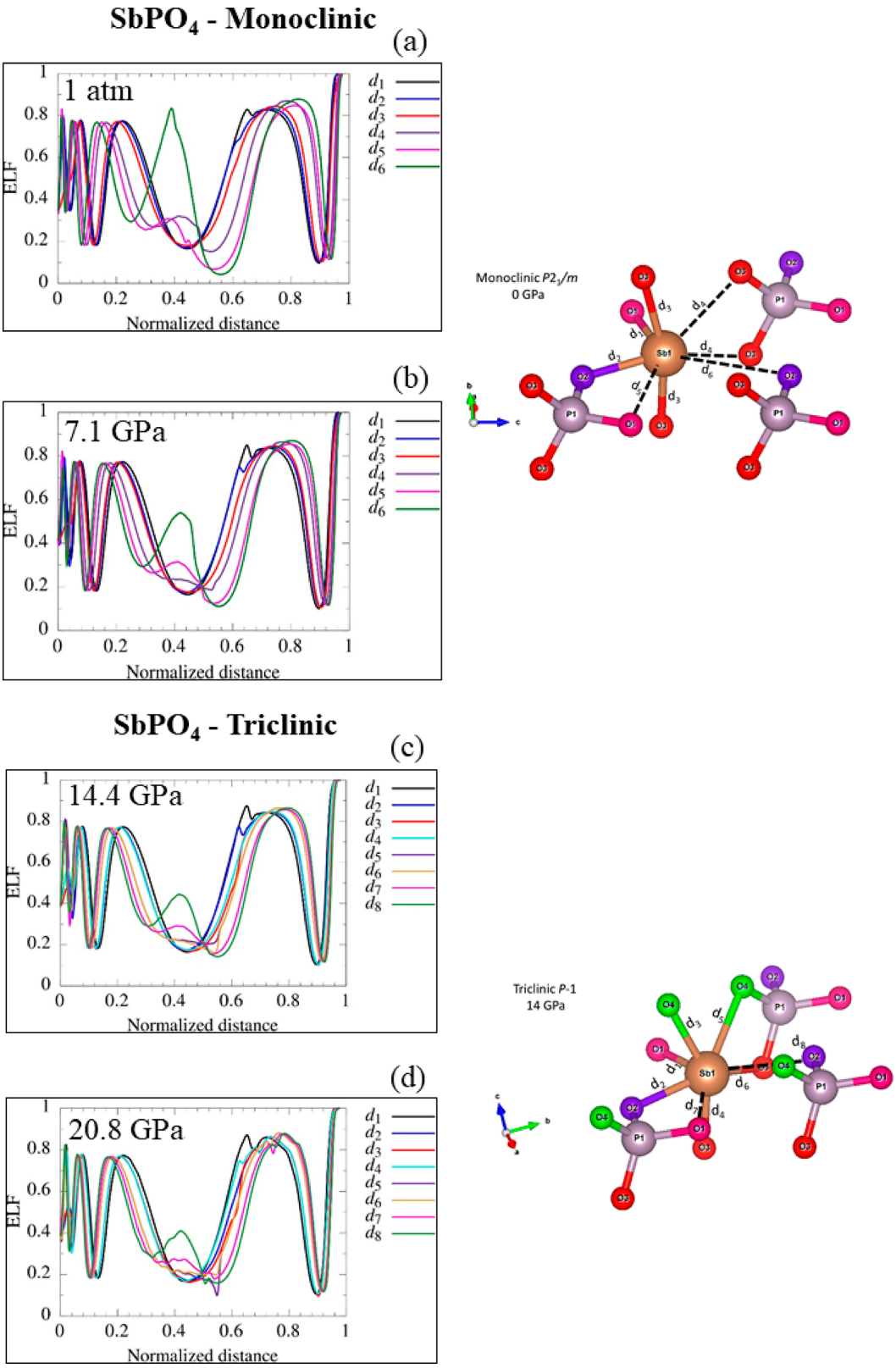


**Figure 13.** Theoretical all-electron 1D-ELF values along the eight shortest Sb−O distances ($d_1$ to $d_6$) in monoclinic $SbPO_4$ at 1 atm (a) and 7.1 GPa (b) and the same for the eight shortest Sb−O distances ($d_1$ to $d_8$) in triclinic $SbPO_4$ at 14.4 GPa (c) and 20.8 GPa (d). Note that both $d_3$ and $d_4$ distances are doubly degenerate in the monoclinic phase, as shown in the structural detail.

pressures, showing that this compound is an indirect band gap material (band gap value above 3.8 eV) that is transparent in the visible, UVA, and UVB spectral regions in the whole pressure range up to 9 GPa.

Theoretical data have helped us to understand the microscopic mechanisms of the compression of monoclinic $SbPO_4$, evidencing that monoclinic $SbPO_4$ undergoes a transition from a 2D-type structure with a 4-fold coordination of Sb at room



DOI: 10.1021/acs.inorgchem.9b02268
Inorg. Chem. XXXX, XXX, XXX−XXX

pressure to a 3D structure with 4 + 2 coordination above 3 GPa. Changes in the Wyckoff positions, changes in the slopes of $c/a$ and $b/a$ ratios, and changes in the pressure dependence of interatomic distances, even of P−O3 bond distances (expected to be rather strong and incompressible bonds), clearly show the occurrence of an IPT around 3 GPa. This IPT is further confirmed by the changes in the pressure coefficients of different vibrational modes around 3 GPa. Moreover, all vibrational modes of $SbPO_4$ that show a negative pressure coefficient at room pressure change to a positive pressure coefficient above 3 GPa. This result is in good agreement with the pressure-induced 2D to 3D phase transition taking place in layered $SbPO_4$ above 3 GPa. The Sb cation increases the coordination number up to (4 + 2 + 1)-fold for the triclinic phase above 15 GPa and the effective coordination of $SbPO_4$ around 18 GPa becomes similar to that of $BiPO_4$-III at room pressure.

Finally, we want to stress that the ability of pressure to modulate the LEP activity and convert the 2D structure of $SbPO_4$ into the 3D network of $BiPO_4$-III may have important implications for technological applications for $SbPO_4$-based compounds, since the role played by external pressure can be mimicked by chemical pressure. In particular, partial substitution of Sb cations in $SbPO_4$ by Bi cations (with smaller LEP) or by other cations with valence 3+ and without an active LEP, such as In, is expected to lead to a closing of the interlayer space of the $SbPO_4$ structure: i.e., it will promote the 3D nature of the compound. Conversely, partial substitution of Sb cations by As cations (with a much stronger LEP) is expected to promote the opening of the structure and consequently the 2D nature of the compound. Thus, our work suggests a way to open or close the structure of layered $SbPO_4$ that can help to enhance the catalytic and atomic-insertion properties of $SbPO_4$-based compounds.

## ■ ASSOCIATED CONTENT

### Supporting Information

The Supporting Information is available free of charge at https://pubs.acs.org/doi/10.1021/acs.inorgchem.9b02268.

Theoretical atomic coordinates of monoclinic ($P2_1/m$) and high-pressure triclinic ($P\bar{1}$) $SbPO_4$, representation of the $SbPO_4$ atomic vibration, angle-dispersive XRD and Raman spectra of $SbPO_4$ measured at different pressures, detail of the monoclinic structure of $SbPO_4$ along the $ac$ plane, evolution of the theoretical Wyckoff positions of monoclinic $SbPO_4$ with pressure, theoretical enthalpy difference vs pressure, evolution of the Sb eccentricity in the $SbO_6$ polyhedron of monoclinic $SbPO_4$, theoretical pressure dependence of the IR-active modes of monoclinic and triclinic $SbPO_4$, and Sb−O distances, charge density, and its Laplacian at the BCPs of the different Sb−O distances in the monoclinic and triclinic phases of $SbPO_4$ at different pressures (PDF)

## ■ AUTHOR INFORMATION


### Corresponding Authors

*E-mail for A.L.d.J.P.: andrepereira@ufgd.edu.br.
*E-mail for F.J.M.: fjmanjon@fis.upv.es.

### ORCID

André Luis de Jesus Pereira: 0000-0003-4757-8080
Rosário Vilaplana: 0000-0003-0504-2157
Daniel Errandonea: 0000-0003-0189-4221
Estelina Lora da Silva: 0000-0002-7093-3266
Alfonso Muñoz: 0000-0003-3347-6518
Plácida Rodríguez-Hernández: 0000-0002-4148-6516
Marcelo Nalin: 0000-0002-7971-6794
Francisco Javier Manjón: 0000-0002-3926-1705


### Notes

The authors declare no competing financial interest.

## ■ ACKNOWLEDGMENTS

The authors acknowledge financial support from the Brazilian Conselho Nacional de Desenvolvimento Científico e Tecnológico (CNPq - 159754/2018-6, 307199/2018-5, 422250/2016-3, 201050/2012-9), FAPESP (2013/07793-6), Spanish Ministerio de Economia y Competitividad (MINECO) under projects MALTA Consolider Ingenio 2010 network (MAT2015-71070-REDC and RED2018-102612-T), MAT2016-75586-C4-1/2/3-P, PGC2018-097520-A-100, FIS2017-83295-P, and PGC2018-094417-B-I00 from Generalitat Valenciana under project PROMETEO/2018/123, and the European Comission under project COMEX. D.S.-P., J.A.S., and A.O.d.l.R. acknowledge "Ramón y Cajal" Fellowships for financial support (RyC-2014-15643, RYC-2015-17482, and RyC-2016-20301, respectively). E.L.d. S., A.M., A.B., and P.R.-H. acknowledge computing time provided by Red Española de Supercomputación (RES) and MALTA-Cluster.

## ■ REFERENCES


(1) Falcão Filho, E. L.; Bosco, C. A. C.; Maciel, G. S.; de Araújo, C. B.; Acioli, L. H.; Nalin, M.; Messaddeq, Y. Ultrafast Nonlinearity of Antimony Polyphosphate Glasses. *Appl. Phys. Lett.* **2003**, *83* (7), 1292−1294.

(2) Nalin, M.; Poulain, M.; Poulain, M.; Ribeiro, S. J. L.; Messaddeq, Y. Antimony Oxide Based Glasses. *J. Non-Cryst. Solids* **2001**, *284* (1−3), 110−116.

(3) Nalin, M.; Messaddeq, Y.; Ribeiro, S. J. L.; Poulain, M.; Briois, V.; Brunklaus, G.; Rosenhahn, C.; Mosel, B. D.; Eckert, H. Structural Organization and Thermal Properties of the Sb2O3 − SbPO4 Glass System. *J. Mater. Chem.* **2004**, *14* (23), 3398−3405.

(4) Montesso, M.; Manzani, D.; Donoso, J. P.; Magon, C. J.; Silva, I. D. A.; Chiesa, M.; Morra, E.; Nalin, M. Synthesis and Structural Characterization of a New SbPO4-GeO2 Glass System. *J. Non-Cryst. Solids* **2018**, *500* (July), 133−140.

(5) Wang, Y.; Li, L.; Li, G. One-Step Synthesis of SbPO4 Hollow Spheres by a Self-Sacrificed Template Method. *RSC Adv.* **2012**, *2* (33), 12999−13006.

(6) Chen, S.; Di, Y.; Li, T.; Li, F.; Cao, W. Impacts of Ionic Liquid Capping on the Morphology and Photocatalytic Performance of SbPO4 Crystals. *CrystEngComm* **2018**, *20* (30), 4305−4312.

(7) Saadaoui, H.; Boukhari, A.; Flandrois, S.; Aride, J. Intercalation of Hydrazine and Amines in Antimony Phosphate. *Mol. Cryst. Liq. Cryst. Sci. Technol., Sect. A* **1994**, *244* (1), 173−178.

(8) Biswal, J. B.; Garje, S. S.; Revaprasadu, N. A Convenient Synthesis of Antimony Sulfide and Antimony Phosphate Nanorods Using Single Source Dithiolatoantimony(III) Dialkyldithiophosphate Precursors. *Polyhedron* **2014**, *80*, 216−222.

(9) Ou, M.; Ling, Y.; Ma, L.; Liu, Z.; Luo, D.; Xu, L. Synthesis and Li-Storage Property of Flower-like SbPO4Microspheres. *Mater. Lett.* **2018**, *224* (April), 100−104.

(10) Jones, P. G.; Sheldrick, G. M.; Schwarzmann, E. Antimony(III) Arsenic(V) Oxide. *Acta Crystallogr., Sect. B: Struct. Crystallogr. Cryst. Chem.* **1980**, *36* (8), 1923−1925.

(11) Kinberger, B.; Danielsen, J.; Haaland, A.; Jerslev, B.; Schäffer, C. E.; Sunde, E.; Sørensen, N. A. The Crystal Structure of SbPO4. *Acta Chem. Scand.* **1970**, *24*, 320−328.




DOI: 10.1021/acs.inorgchem.9b02268
*Inorg. Chem.* XXXX, XXX, XXX−XXX

(12) Achary, S. N.; Errandonea, D.; Muñoz, A.; Rodríguez-Hernández, P.; Manjón, F. J.; Krishna, P. S. R.; Patwe, S. J.; Grover, V.; Tyagi, A. K. Experimental and Theoretical Investigations on the Polymorphism and Metastability of BiPO4. *Dalt. Trans.* **2013**, *42* (42), 14999−15015.
(13) Alonzo, G.; Bertazzi, N.; Galli, P.; Marci, G.; Massucci, M. A.; Palmisano, L.; Patrono, P.; Saiano, F. In Search of Layered Antimony(III) Materials: Synthesis and Characterization of Oxo-Antimony(III) Catecholate and Further Studies on Antimony(III) Phosphate. *Mater. Res. Bull.* **1998**, *33* (8), 1233−1240.
(14) Alonzo, G.; Bertazzi, N.; Galli, P.; Massucci, M. A.; Patrono, P.; Saiano, F. On the Synthesis and Characterization of Layered Antimony(III) Phosphate and Its Interaction with Moist Ammonia and Amines. *Mater. Res. Bull.* **1998**, *33* (8), 1221−1231.
(15) Brockner, W.; Hoyer, L. P. Synthesis and Vibrational Spectrum of Antimony Phosphate, SbPO4. *Spectrochim. Acta, Part A* **2002**, *58* (9), 1911−1914.
(16) Sudarsan, V.; Muthe, K. P.; Vyas, J. C.; Kulshreshtha, S. K. PO43- Tetrahedra in SbPO4 and SbOPO4: A 31P NMR and XPS Study. *J. Alloys Compd.* **2002**, *336* (1−2), 119−123.
(17) Errandonea, D.; Gomis, O.; Santamaría-Perez, D.; García-Domene, B.; Muñoz, A.; Rodríguez-Hernández, P.; Achary, S. N.; Tyagi, A. K.; Popescu, C. Exploring the High-Pressure Behavior of the Three Known Polymorphs of BiPO4: Discovery of a New Polymorph. *J. Appl. Phys.* **2015**, *117* (10), 105902.
(18) Lacomba-Perales, R.; Errandonea, D.; Meng, Y.; Bettinelli, M. High-Pressure Stability and Compressibility of A PO4 (A = La, Nd, Eu, Gd, Er, and Y) Orthophosphates: An x-Ray Diffraction Study Using Synchrotron Radiation. *Phys. Rev. B: Condens. Matter Mater. Phys.* **2010**, *81* (6), 1−9.
(19) Errandonea, D.; Gomis, O.; Rodríguez-Hernández, P.; Muñoz, A.; Ruiz-Fuertes, J.; Gupta, M.; Achary, S. N.; Hirsch, A.; Manjon, F. J.; Peters, L.; et al. High-Pressure Structural and Vibrational Properties of Monazite-Type BiPO 4, LaPO 4, CePO 4, and PrPO 4. *J. Phys.: Condens. Matter* **2018**, *30* (6), 065401.
(20) López-Solano, J.; Rodríguez-Hernández, P.; Muñoz, A.; Gomis, O.; Santamaría-Perez, D.; Errandonea, D.; Manjón, F. J.; Kumar, R. S.; Stavrou, E.; Raptis, C. Theoretical and Experimental Study of the Structural Stability of TbPO 4 at High Pressures. *Phys. Rev. B: Condens. Matter Mater. Phys.* **2010**, *81* (14), 1−9.
(21) Musselman, M. A.; Wilkinson, T. M.; Haberl, B.; Packard, C. E. In Situ Raman Spectroscopy of Pressure-induced Phase Transformations in Polycrystalline $TbPO_4$, $DyPO_4$, and $Gd_xDy_{(1-x)}PO_4$. *J. Am. Ceram. Soc.* **2018**, *101* (6), 2562−2570.
(22) Muñoz, A.; Rodríguez-Hernández, P. High-Pressure Elastic, Vibrational and Structural Study of Monazite-Type GdPO4 from Ab Initio Simulations. *Crystals* **2018**, *8* (5), 209.
(23) Ghosh, P. S.; Ali, K.; Arya, A. A Computational Study of High Pressure Polymorphic Transformations in Monazite-Type LaPO 4. *Phys. Chem. Chem. Phys.* **2018**, *20* (11), 7621−7634.
(24) Gomis, O.; Lavina, B.; Rodríguez-Hernández, P.; Muñoz, A.; Errandonea, R.; Errandonea, D.; Bettinelli, M. High-Pressure Structural, Elastic, and Thermodynamic Properties of Zircon-Type HoPO4 and TmPO4. *J. Phys.: Condens. Matter* **2017**, *29* (9), 095401.
(25) Ruiz-Fuertes, J.; Hirsch, A.; Friedrich, A.; Winkler, B.; Bayarjargal, L.; Morgenroth, W.; Peters, L.; Roth, G.; Milman, V. High-Pressure Phase of LaPO4 Studied by x-Ray Diffraction and Second Harmonic Generation. *Phys. Rev. B: Condens. Matter Mater. Phys.* **2016**, *94* (13), 1−6.
(26) Stavrou, E.; Tatsi, A.; Raptis, C.; Efthimiopoulos, I.; Syassen, K.; Muñoz, A.; Rodríguez-Hernández, P.; López-Solano, J.; Hanfland, M. Effects of Pressure on the Structure and Lattice Dynamics of TmPO4: Experiments and Calculations. *Phys. Rev. B: Condens. Matter Mater. Phys.* **2012**, *85* (2), 1−12.
(27) Errandonea, D.; Garg, A. B. Recent Progress on the Characterization of the High-Pressure Behaviour of AVO 4 Orthovanadates. *Prog. Mater. Sci.* **2018**, *97* (April), 123−169.
(28) Bandiello, E.; Errandonea, D.; Pellicer-Porres, J.; Garg, A. B.; Rodriguez-Hernandez, P.; Muñoz, A.; Martinez-Garcia, D.; Rao, R.; Popescu, C. Effect of High Pressure on the Crystal Structure and Vibrational Properties of Olivine-Type LiNiPO 4. *Inorg. Chem.* **2018**, *57* (16), 10265−10276.
(29) Achary, S. N.; Bevara, S.; Tyagi, A. K. Recent Progress on Synthesis and Structural Aspects of Rare-Earth Phosphates. *Coord. Chem. Rev.* **2017**, *340*, 266−297.
(30) Bykov, M.; Bykova, E.; Hanfland, M.; Liermann, H. P.; Kremer, R. K.; Glaum, R.; Dubrovinsky, L.; van Smaalen, S. High-Pressure Phase Transformations in TiPO 4 : A Route to Pentacoordinated Phosphorus. *Angew. Chem., Int. Ed.* **2016**, *55* (48), 15053−15057.
(31) López-Moreno, S.; Errandonea, D. Ab Initio Prediction of Pressure-Induced Structural Phase Transitions of CrVO 4-Type Orthophosphates. *Phys. Rev. B: Condens. Matter Mater. Phys.* **2012**, *86* (10), 1−14.
(32) Errandonea, D.; Manjón, F. J. Pressure Effects on the Structural and Electronic Properties of ABX4 Scintillating Crystals. *Prog. Mater. Sci.* **2008**, *53* (4), 711−773.
(33) Merrill, L.; Bassett, W. A. Miniature Diamond Anvil Pressure Cell for Single Crystal X-Ray Diffraction Studies. *Rev. Sci. Instrum.* **1974**, *45* (2), 290−294.
(34) Fauth, F.; Peral, I.; Popescu, C.; Knapp, M. The New Material Science Powder Diffraction Beamline at ALBA Synchrotron. *Powder Diffr.* **2013**, *28* (S2), S360−S370.
(35) Mao, H. K.; Xu, J.; Bell, P. M. Calibration of the Ruby Pressure Gauge to 800 Kbar under Quasi-Hydrostatic Conditions. *J. Geophys. Res.* **1986**, *91* (B5), 4673.
(36) Dewaele, A.; Loubeyre, P.; Mezouar, M. Equations of State of Six Metals above 94 GPa. *Phys. Rev. B: Condens. Matter Mater. Phys.* **2004**, *70* (9), 1−8.
(37) Prescher, C.; Prakapenka, V. B. DIOPTAS: A Program for Reduction of Two-Dimensional X-Ray Diffraction Data and Data Exploration. *High Pressure Res.* **2015**, *35* (3), 223−230.
(38) Rodríguez-Carvajal, J. Recent Advances in Magnetic Structure Determination by Neutron Powder Diffraction. *Phys. B* **1993**, *192* (1−2), 55−69.
(39) Nolze, G.; Kraus, W. PowderCell 2.0 for Windows. *Powder Diffr.* **2016**, *13*, 256−259.
(40) Errandonea, D.; Muñoz, A.; Gonzalez-Platas, J. Comment on High-Pressure x-Ray Diffraction Study of YBO3/Eu 3+, GdBO3, and EuBO3: Pressure-Induced Amorphization in GdBO3. *J. Appl. Phys.* **2014**, *115* (21), 113−116.
(41) Hohenberg, P.; Kohn, W. Inhomogeneous Electron Gas. *Phys. Rev.* **1964**, *136* (3B), B864−B871.
(42) Kresse, G.; Hafner, J. *Ab Initio* Molecular Dynamics for Liquid Metals. *Phys. Rev. B: Condens. Matter Mater. Phys.* **1993**, *47* (1), 558−561.
(43) Blöchl, P. E. Projector Augmented-Wave Method. *Phys. Rev. B: Condens. Matter Mater. Phys.* **1994**, *50* (24), 17953−17979.
(44) Perdew, J. P.; Ruzsinszky, A.; Csonka, G. I.; Vydrov, O. A.; Scuseria, G. E.; Constantin, L. A.; Zhou, X.; Burke, K. *Phys. Rev. Lett.* **2008**, *100*, 136406.
(45) Monkhorst, H. J.; Pack, J. D. Special Points Fro Brillouin-Zone Integretions. *Phys. Rev. B* **1976**, *13* (12), 5188−5192.
(46) Parlinski, K. Computer Code PHONON; http://wolf.ifj.edu.pl/phonon.
(47) Nielsen, O. H.; Martin, R. M. Quantum-Mechanical Theory of Stress and Force. *Phys. Rev. B: Condens. Matter Mater. Phys.* **1985**, *32* (6), 3780−3791.
(48) Le Page, Y.; Saxe, P. Symmetry-General Least-Squares Extraction of Elastic Data for Strained Materials from *Ab Initio* Calculations of Stress. *Phys. Rev. B: Condens. Matter Mater. Phys.* **2002**, *65* (10), 104104.
(49) Otero-De-La-Roza, A.; Johnson, E. R.; Luaña, V. Critic2: A Program for Real-Space Analysis of Quantum Chemical Interactions in Solids. *Comput. Phys. Commun.* **2014**, *185* (3), 1007−1018.
(50) Bader, R. F. W. *Atoms in Molecules. A Quantum Theory*; Clarendon Press - Oxford, 1994.
(51) Dewhurst, K.; Sharma, S.; Nordström, L.; Cricchio, F.; Grånäs, O.; Gross, H.; Ambrosch-Draxl, C.; Persson, C.; Bultmark, F.; Brouder,


DOI: 10.1021/acs.inorgchem.9b02268
*Inorg. Chem.* XXXX, XXX, XXX−XXX

C., et al. The Elk FP-LAPW code; http://elk.sourceforge.net/ (accessed Oct 31, 2019).
(52) Manjón, F. J.; Vilaplana, R.; Gomis, O.; Pérez-González, E.; Santamaría-Pérez, D.; Marín-Borrás, V.; Segura, A.; González, J.; Rodríguez-Hernández, P.; Muñoz, A.; et al. High-Pressure Studies of Topological Insulators Bi2Se3, Bi2Te3, and Sb2Te3. *Phys. Status Solidi B* **2013**, *250* (4), 669−676.
(53) Pereira, A. L. J.; Errandonea, D.; Beltrán, A.; Gracia, L.; Gomis, O.; Sans, J. A.; García-Domene, B.; Miquel-Veyrat, A.; Manjón, F. J.; Muñoz, A. Structural Study of $\alpha$-Bi2O3 under Pressure. *J. Phys.: Condens. Matter* **2013**, *25* (47), 475402.
(54) Pereira, A. L. J.; Sans, O. G. J. A.; Manjón, F. J. Pressure Effects on the Vibrational Properties of $\alpha$-Bi2O3 : An Experimental and Theoretical Study. *J. Phys.: Condens. Matter* **2014**, *26*, 225401.
(55) Pereira, A. L. J.; Sans, J. A.; Vilaplana, R.; Gomis, O.; Manjón, F. J.; Rodríguez-Hernández, P.; Muñoz, A.; Popescu, C.; Beltrán, A. Isostructural Second-Order Phase Transition of $\beta$-Bi2O3 at High Pressures: An Experimental and Theoretical Study. *J. Phys. Chem. C* **2014**, *118* (40), 23189−23201.
(56) Ibáñez, J.; Sans, J. A.; Popescu, C.; López-Vidrier, J.; Elvira-Betanzos, J. J.; Cuenca-Gotor, V. P.; Gomis, O.; Manjón, F. J.; Rodríguez-Hernández, P.; Muñoz, A. Structural, Vibrational, and Electronic Study of Sb2S3 at High Pressure. *J. Phys. Chem. C* **2016**, *120* (19), 10547−10558.
(57) Kroumova, E.; Aroyo, M. L.; Perez-Mato, J. M.; Kirov, A.; Capillas, C.; Ivantchev, S.; Wondratschek, H. Bilbao Crystallographic Server: Useful Databases and Tools for Phase-Transition Studies. *Phase Transitions* **2003**, *76* (1−2), 155−170.
(58) Canepa, P.; Hanson, R. M.; Ugliengo, P.; Alfredsson, M. J-ICE : A New Jmol Interface for Handling and Visualizing Crystallographic and Electronic Properties. *J. Appl. Crystallogr.* **2011**, *44* (1), 225−229.
(59) Sans, J. A.; Manjón, F. J.; Pereira, A. L. J.; Vilaplana, R.; Gomis, O.; Segura, A.; Muñoz, A.; Rodríguez-Hernández, P.; Popescu, C.; Drasar, C.; et al. Structural, Vibrational, and Electrical Study of Compressed BiTeBr. *Phys. Rev. B: Condens. Matter Mater. Phys.* **2016**, *93* (2), 1−11.
(60) Pereira, A. L. J.; Santamaría-Pérez, D.; Ruiz-Fuertes, J.; Manjón, F. J.; Cuenca-Gotor, V. P.; Vilaplana, R.; Gomis, O.; Popescu, C.; Munoz, A.; Rodríguez-Hernández, P.; et al. Experimental and Theoretical Study of Bi2O2Se under Compression. *J. Phys. Chem. C* **2018**, *122* (16), 8853−8867.
(61) Nakamoto, K. *Infrared and Raman Spectra of Inorganic and Coordination Compounds, Part A: Theory and Applications in Inorganic Chemistry*, 6th ed.; Wiley: New York, 2009.
(62) Bai, Y.; Srikanth, N.; Chua, C. K.; Zhou, K. Density Functional Theory Study of Mn+1AXn Phases: A Review. *Crit. Rev. Solid State Mater. Sci.* **2019**, *44* (1), 56−107.
(63) Bai, Y.; He, X.; Wang, R.; Zhu, C. An Ab Initio Study on Compressibility of Al-Containing MAX-Phase Carbides. *J. Appl. Phys.* **2013**, *114* (17), 173709.
(64) Bai, Y.; Qi, X.; He, X.; Sun, D.; Kong, F.; Zheng, Y.; Wang, R.; Duff, A. I. Phase Stability and Weak Metallic Bonding within Ternary-Layered Borides CrAlB, Cr2AlB2, Cr3AlB4, and Cr4AlB6. *J. Am. Ceram. Soc.* **2019**, *102* (6), 3715−3727.
(65) Birch, F. Finite Strain Isotherm and Velocities for Single-Crystal and Polycrystalline NaCl at High Pressures and 300 K. *J. Geophys. Res.* **1978**, *83* (B3), 1257.
(66) Pereira, A. L. J.; Gomis, O.; Sans, J. A. $\beta$ -Bi2O3 under Compression : Optical and Elastic Properties and Electron Density Topology Analysis. *Phys. Rev. B: Condens. Matter Mater. Phys.* **2016**, *93*, 224111.
(67) Cuenca-Gotor, V. P.; Sans, J. A.; Ibáñez, J.; Popescu, C.; Gomis, O.; Vilaplana, R.; Manjón, F. J.; Leonardo, A.; Sagasta, E.; Suárez-Alcubilla, A.; et al. Structural, Vibrational, and Electronic Study of $\alpha$-As2Te3 under Compression. *J. Phys. Chem. C* **2016**, *120* (34), 19340−19352.
(68) Korabel'nikov, D. V.; Zhuravlev, Y. N. Structural, Elastic, Electronic and Vibrational Properties of a Series of Sulfates from First Principles Calculations. *J. Phys. Chem. Solids* **2018**, *119*, 114−121.
(69) Santamaría-Pérez, D.; Gracia, L.; Garbarino, G.; Beltrán, A.; Chuliá-Jordán, R.; Gomis, O.; Errandonea, D.; Ferrer-Roca, C.; Martínez-García, D.; Segura, A. High-Pressure Study of the Behavior of Mineral Barite by x-Ray Diffraction. *Phys. Rev. B: Condens. Matter Mater. Phys.* **2011**, *84* (5), 1−8.
(70) Santamaria-Perez, D.; Chulia-Jordan, R.; Daisenberger, D.; Rodriguez-Hernandez, P.; Munỳoz, A. Dense Post-Barite-Type Polymorph of PbSO4 Anglesite at High Pressures. *Inorg. Chem.* **2019**, *58* (4), 2708−2716.
(71) Hinrichsen, B.; Dinnebier, R. E.; Liu, H.; Jansen, M. The High Pressure Crystal Structures of Tin Sulphate: A Case Study for Maximal Information Recovery from 2D Powder Diffraction Data. *Zeitschrift fur Krist.* **2008**, *223* (3), 195−203.
(72) Knight, K. S. Analytical Expressions to Determine the Isothermal Compressibility Tensor and the Isobaric Thermal Expansion Tensor for Monoclinic Crystals: Application to Determine the Direction of Maximum Compressibility in Jadeite. *Phys. Chem. Miner.* **2010**, *37* (8), 529−533.
(73) Angel, R. J. Win_Strain; http://www.rossangel.com/text_strain.htm.
(74) Errandonea, D.; Muñoz, A.; Rodríguez-Hernández, P.; Gomis, O.; Achary, S. N.; Popescu, C.; Patwe, S. J.; Tyagi, A. K. High-Pressure Crystal Structure, Lattice Vibrations, and Band Structure of BiSbO4. *Inorg. Chem.* **2016**, *55* (10), 4958−4969.
(75) Bodenstein, D.; Brehm, A.; Jones, P. G.; Schwarzmann, E.; Sheldrick, G. M. Darstellung Und Kristallstruktur von Arsen(III)-Phosplior(V)Oxid, AsPO4/Preparation and Crystal Structure of Arsenic(III) Phosphorus(V) Oxide, AsPO4. *Z. Naturforsch., B: J. Chem. Sci.* **1982**, *37* (2), 136−137.
(76) Ruiz-Fuertes, J.; Friedrich, A.; Gomis, O.; Errandonea, D.; Morgenroth, W.; Sans, J. A.; Santamaría-Pérez, D. High-Pressure Structural Phase Transition in MnWO4. *Phys. Rev. B: Condens. Matter Mater. Phys.* **2015**, *91* (10), 1−7.
(77) Garg, A. B.; Errandonea, D.; Rodríguez-Hernández, P.; Muñoz, A. ScVO4 under Non-Hydrostatic Compression: A New Metastable Polymorph. *J. Phys.: Condens. Matter* **2017**, *29* (5), 055401.
(78) Momma, K.; Izumi, F. VESTA 3 for Three-Dimensional Visualization of Crystal, Volumetric and Morphology Data. *J. Appl. Crystallogr.* **2011**, *44* (6), 1272−1276.
(79) Hoppe, R. The Coordination Number− an"Inorganic Chameleon. *Angew. Chem., Int. Ed. Engl.* **1970**, *9* (1), 25−34.
(80) Hoppe, R. Effective Coordination Numbers (ECoN) and Mean Fictive Ionic Radii (MEFIR) [1,2]. *Z. Kristallogr. - Cryst. Mater.* **1979**, *150* (1−4), 23−52.
(81) Baur, W. H. The Geometry of Polyhedral Distortions. Predictive Relationships for the Phosphate Group. *Acta Crystallogr., Sect. B: Struct. Crystallogr. Cryst. Chem.* **1974**, *30* (5), 1195−1215.
(82) Guńka, P. A.; Zachara, J. Towards a Quantitative Bond Valence Description of Coordination Spheres − the Concepts of Valence Entropy and Valence Diversity Coordination Numbers. *Acta Crystallogr., Sect. B: Struct. Sci., Cryst. Eng. Mater.* **2019**, *75* (1), 86−96.
(83) Ruiz-Fuertes, J.; Segura, A.; Rodríguez, F.; Errandonea, D.; Sanz-Ortiz, M. N. Anomalous High-Pressure Jahn-Teller Behavior in CuWO4. *Phys. Rev. Lett.* **2012**, *108* (16), 23−26.
(84) Pellicer-Porres, J.; Saitta, A. M.; Polian, A.; Itié, J. P.; Hanfland, M. Six-Fold-Coordinated Phosphorus by Oxygen in AlPO4 Quartz Homeotype under High Pressure. *Nat. Mater.* **2007**, *6* (9), 698−702.
(85) Angot, E.; Huang, B.; Levelut, C.; Le Parc, R.; Hermet, P.; Pereira, A. S.; Aquilanti, G.; Frapper, G.; Cambon, O.; Haines, J. Experimental and First-Principles Calculation Study of the Pressure-Induced Transitions to a Metastable Phase in GaPO4 and in the Solid Solution AlPO4−GaPO4. *Phys. Rev. Mater.* **2017**, *1* (3), 033607.
(86) Stavrou, E.; Tatsi, A.; Salpea, E.; Boulmetis, Y. C.; Kontos, A. G.; Raptis, Y. S.; Raptis, C. Raman Study of Zircon-Structured RPO4 (R = Y, Tb, Er, Tm) Phosphates at High Pressures. *J. Phys. Conf. Ser.* **2008**, *121* (4), 042016.
(87) Tatsi, A.; Stavrou, E.; Boulmetis, Y. C.; Kontos, A. G.; Raptis, Y. S.; Raptis, C. Raman Study of Tetragonal TbPO4 and Observation of a


DOI: 10.1021/acs.inorgchem.9b02268
*Inorg. Chem.* XXXX, XXX, XXX−XXX

First-Order Phase Transition at High Pressure. *J. Phys.: Condens. Matter* **2008**, *20* (42), 425216.
(88) Zhang, F. X.; Wang, J. W.; Lang, M.; Zhang, J. M.; Ewing, R. C.; Boatner, L. A. High-Pressure Phase Transitions of ScPO4 and YPO4. *Phys. Rev. B: Condens. Matter Mater. Phys.* **2009**, *80* (18), 1−7.
(89) Vilaplana, R.; Santamaría-Pérez, D.; Gomis, O.; Manjón, F. J.; González, J.; Segura, A.; Muñoz, A.; Rodríguez-Hernández, P.; Pérez-González, E.; Marín-Borrás, V.; et al. Structural and Vibrational Study of Bi2Se3 under High Pressure. *Phys. Rev. B: Condens. Matter Mater. Phys.* **2011**, *84* (18), 184110.



DOI: 10.1021/acs.inorgchem.9b02268
*Inorg. Chem.* XXXX, XXX, XXX−XXX